Universidade Federal de Uberlândia

Instituto de Física

Lucas Soares Sousa

RKKY interaction in topological nanoribbons: a DMRG study

Uberlândia - MG

2024

Lucas Soares Sousa

RKKY interaction in topological nanoribons: a DMRG study

Dissertação de mestrado apresentado ao Instituto de Física da Universidade Federal de Uberlândia como requisito parcial para obtenção do título de mestre em Física.

Orientador: Prof. Dr. George Balster Martins
Coorientador: Prof. Dr. Adrian Feiguin

Uberlândia - MG
2024

Ficha Catalográfica Online do Sistema de Bibliotecas da UFU
com dados informados pelo(a) próprio(a) autor(a).

S725 Sousa, Lucas Soares, 1998-
2024 RKKY interaction in topological nanoribons: a DMRG study [recurso eletrônico] / Lucas Soares Sousa. - 2024.

Orientador: George Martins.
Coorientador: Adrian Feiguin.
Tese (Doutorado) - Universidade Federal de Uberlândia, Pós-graduação em Física.
Modo de acesso: Internet.
Disponível em: http://doi.org/10.14393/ufu.te.2024.667
Inclui bibliografia.
Inclui ilustrações.

1. Física. I. Martins, George,1962-, (Orient.). II. Feiguin, Adrian, -, (Coorient.). III. Universidade Federal de Uberlândia. Pós-graduação em Física. IV. Título.

CDU: 53

Bibliotecários responsáveis pela estrutura de acordo com o AACR2:

Gizele Cristine Nunes do Couto - CRB6/2091
Nelson Marcos Ferreira - CRB6/3074

UNIVERSIDADE FEDERAL DE UBERLÂNDIA
Coordenação do Programa de Pós-Graduação em Física
Av. João Naves de Ávila, 2121, Bloco 1A, Sala 213 - Bairro Santa Mônica, Uberlândia-MG, CEP 38400-902
Telefone: (34) 3239-4309 - www.infis.ufu.br - cpgfisica@ufu.br

ATA DE DEFESA - PÓS-GRADUAÇÃO

Programa de Pós-Graduação em:	Física				
Defesa de:	Dissertação de Mestrado				
Data:	02 de agosto de 2024	Hora de início:	14:00	Hora de encerramento:	16:10
Matrícula do Discente:	12222FIS004				
Nome do Discente:	Lucas Soares Sousa				
Título do Trabalho:	RKKY interaction in topological nanoribons: a DMRG study				
Área de concentração:	Física				
Linha de pesquisa:	Sistemas nanoestruturados				
Projeto de Pesquisa de vinculação:	N.A				

Reuniu-se por meio de videoconferencia, a Banca Examinadora, designada pelo Colegiado do Programa de Pós-graduação em Física da Universidade Federal de Uberlândia - UFU, assim composta: Professores Doutores: Gerson Ferreira Júnior - INFIS/UFU, Mucio Amado Continentine - CBPF e George Balster Martins - INFIS/UFU, presidente da banca.

Iniciando os trabalhos o presidente da mesa, Prof. George Balster Martins apresentou a Comissão Examinadora e o candidato, agradeceu a presença do público, e concedeu ao discente a palavra para a exposição do seu trabalho. A duração da apresentação do Discente e o tempo de arguição e resposta foram conforme as normas do Programa.

A seguir o senhor(a) presidente concedeu a palavra, pela ordem sucessivamente, aos(às) examinadores(as), que passaram a arguir o(a) candidato(a). Ultimada a arguição, que se desenvolveu dentro dos termos regimentais, a Banca, em sessão secreta, atribuiu o resultado final, considerando o(a) candidato(a):

Aprovado

Esta defesa faz parte dos requisitos necessários à obtenção do título de Mestre.

O competente diploma será expedido após cumprimento dos demais requisitos, conforme as normas do Programa, a legislação pertinente e a regulamentação interna da UFU.

Nada mais havendo a tratar foram encerrados os trabalhos. Foi lavrada a presente ata que após lida e achada conforme foi assinada pela Banca Examinadora.

Documento assinado eletronicamente por **Gerson Ferreira Junior**, **Professor(a) do Magistério Superior**, em 05/08/2024, às 07:41, conforme horário oficial de Brasília, com fundamento no art. 6º, § 1º, do Decreto nº 8.539, de 8 de outubro de 2015.

Documento assinado eletronicamente por **George Balster Martins**, **Professor(a) do Magistério Superior**, em 05/08/2024, às 07:42, conforme horário oficial de Brasília, com fundamento no art. 6º, § 1º, do Decreto nº 8.539, de 8 de outubro de 2015.

Documento assinado eletronicamente por **Múcio Amado Continentino**, **Usuário Externo**, em 05/08/2024, às 22:09, conforme horário oficial de Brasília, com fundamento no art. 6º, § 1º, do Decreto nº 8.539, de 8 de outubro de 2015.

A autenticidade deste documento pode ser conferida no site https://www.sei.ufu.br/sei/controlador_externo.php?acao=documento_conferir&id_orgao_acesso_externo=0, informando o código verificador **5576883** e o código CRC **3E58CCB8**.

Referência: Processo nº 23117.049121/2024-23 SEI nº 5576883

Acknowledgements

First of all, I would like to thank my parents for everything they have always done for me, all the struggles, all the dedication and encouragement they have had for me and my little sister, who is now one of the greatest joys of my life.

I thank the people who have always been by my side these last few years, especially my great friends and people who have always been by my side, especially Rafaela.

I thank my Advisor Professor George for the guidance and all the knowledge I gained throughout this process, and to my co-advisor both for the learning about DMRG that I obtained with it and for the availability of its codes to calculate the results present in this work.

Finally, I would like to thank INFIS and PPFIS for the opportunity and CAPES, FAPEMIG, and CNPQ for their financial support.

Resumo

O estudo do modelo de Anderson de duas impurezas possui um posição proeminente na tentativa de compreender a física de materiais com férmions pesados. Como no caso dos férmions pesados, um sistema de duas impurezas pode apresentar uma competição entre os acoplamentos Kondo e Ruderman-Kittel-Kasuya-Yosida (RKKY). O primeiro é o acoplamento entre um momento magnético localizado (em um hospedeiro metálico) e os elétrons de condução. O chamado efeito Kondo é caracterizado pela blindagem (formação de um singleto) do momento magnético da impureza pelos elétrons de condução. A interação RKKY é uma interação indireta entre duas impurezas magnéticas, mediada pelos elétrons de condução. Nesta dissertação, estudamos a interação RKKY entre duas impurezas que estão conectadas por um estado de borda metálico topológico em uma nanofita de siliceno. Usamos a transformação de Lanczos mais o método DMRG para tratar este problema numericamente. Além de encontrar concordância parcial com os cálculos da teoria quântica de campos, fazemos um exame minucioso da convergência dos resultados com os parâmetros DMRG.

Palavras-chave: isolantes topológicos, nanofitas de siliceno, interação RKKY.

Abstract

The study of the two-impurity Anderson model has a prominent position in the attempt to understand the physics of heavy-fermion materials. As in the case with heavy-fermions, a two impurity system may present a competition between the Kondo and the Ruderman-Kittel-Kasuya-Yosida (RKKY) couplings. The first is the coupling between a localized magnetic moment (in a metallic host) and the conduction electrons. The so-called Kondo effect is characterized by the screening (singlet formation) of the impurity magnetic moment by the conduction electrons. The RKKY interaction is an indirect interaction between two magnetic impurities, mediated by the conduction electrons. In this dissertation, we study the RKKY interaction between two impurities that are connected by a topological metallic edge state in a silicene nanoribbon. We use the Lanczos transformation plus DMRG method to treat this problem numerically. Besides finding partial agreement with quantum field theory calculations, we do a thorough examination of the convergence of the results with the DMRG parameters.

Keywords: topological insulators, silicene nanoribbons, RKKY interaction.

List of Figures

Contents

1 Introduction

1.1 Context

It is well-known that magnetic impurities, when diluted in small concentrations in a metallic host, impart singular characteristics to its properties, most notably its resistivity, which acquires a minimum as a function of temperature [2]. This phenomenon, first observed in the mid 1930s [3], was given a satisfactory explanation only in 1964 by Jun Kondo [4]: the localized magnetic moment of the impurity [5] is screened by the spins of the conduction electrons below a characteristic temperature, the so-called Kondo temperature T_K [6]. The Kondo effect holds a prominent place in many body-physics, since it was one of the earliest manifestations of many-body effects in condensed matter [7, 8]. The phenomenon was only fully understood after the development of Numerical Renormalization Group ideas [9, 10, 11].

Heavy fermion (HF) materials [12, 13] also hold a prominent position in the study of many-body physics, since the observation, in 1975, of a remarkably high linear specific heat capacity in $CeAl_3$ [14]. One universal characteristic of the HF materials is the presence of rare-earth (actinide) ions, i.e., incomplete $4f$ ($5f$) shells, in their composition [1]. It soon became clear that the phenomenology of the HFs originated in the competition between the Kondo [2] and the Ruderman-Kittel-Kasuya-Yosida (RKKY) [15, 16, 17] energy scales. The RKKY interaction is a long-range interaction between magnetic moments [5] in metals (in the case of HFs, the localized magnetic moments of the 4f or 5f electrons in the rare-earth or actinide ions, respectively). That interaction arises when conduction electrons in a metal mediate a coupling between those localized magnetic moments. The strength of this interaction oscillates with the distance between the magnetic moments and decays inversely with it.

The simplest system that shows the competition between Kondo and RKKY contains only two magnetic impurities in a metallic host. This system has been extensively studied theoretically when the host is a 'traditional' metal [18, 19]. Much less is known when the host has non-trivial topological properties, showing metallic states only on its surface. One of such systems is silicene [1], a two-dimensional material. In this dissertation, we use the Lanczos transformation plus Density Matrix Renormalization Group (DMRG) [20] to study the RKKY interaction between two impurities adsorbed onto the edge of a silicene nanoribbons. We find that the intrinsic spin-orbit interaction present in silicene causes a strong anisotropy in the spin correlations between the magnetic impurities. In addition,

[1] For example, the most studied HFs are $CeCoIn_5$, $YbAl_3$, UBe_13, UPt_3, etc.

we also analyze how the correlations change with the variation of the parameters in the Anderson model (mostly Hubbard U).

Recently, interest in RKKY has been growing due to its potential applications in nanotechnology, most notably in giant magnetoresistance (GMR) devices, in which an increase in the magnetoresistance (change in the electric resistance due to the presence of a magnetic field) is observed in multi-layers composed of alternating ferromagnetic and non-magnetic conductive layers [21, 22]. The main applications of GMR is in the data storage industry, specially in hard disk and magnetic field sensors.

1.2 Motivation and related works

Some groups [23, 24] argue that the RKKY interaction and the RKKY vs Kondo competition become nontrivial on helical edges of two-dimensional topological insulators, where there is a lock-in between the electron spin and its momentum. Quantum field theory calculations suggest that the one-dimensionality and the helicity of the metallic edge-channel result in that the Kondo screening always dominates at large inter-impurity distances and even at short distances, if the Kondo coupling is sufficiently large and anisotropic.

Indeed, in Refs. [23, 24] it was suggested that the paradigmatic RKKY approach [15, 16, 17] breaks down in strongly correlated helical systems, or so-called helical Luttinger liquids. Yevtushenko et al. [23, 24] argue that the reason for this unexpected result is the nontrivial, and unusually increased, RKKY vs Kondo competition.

The origin of the behavior described by the references mentioned above rests in Luttinger liquid physics [25], which centers in the fact that, because of interactions (even weak), a free-electron-like metal will not be stable in one-dimension. In other words, in a one-dimensional metal, correlations are strong even for weak interactions.

Here, we complement the work by Yevtushenko's group [23, 24] by treating a non-interacting host (thus, its edge channel is not a Luttinger liquid). This allows us to try to ascertain how much of the effects seen in the interacting theory really depend on the host interactions. An added benefit of our calculations is that our model possesses real space resolution, while the Luttinger liquid model does not.

Our preliminary results seem to confirm that interactions are the cause of the unusual behavior observed by Yevtushenko et al. [23, 24], although the spatial resolution in our calculations (difference between Crest and Trough sites, see below) precludes a straightforward interpretation of the results.

This dissertation is organized as follows. In Chapter 2 we discuss the edge states in silicene zigzag nanoribbons. In Chapter 3 we give a brief introduction to the Kondo

effect and the RKKY interaction, while in Chapter 4 we present the methods used in the calculations, viz., the Lanczos Transformation and the DMRG method. In Chapter 5, besides providing a careful analysis of the convergence of the DMRG results, we present our results for the RKKY interaction in silicene nanoribbons, while in Chapter 6 we present our conclusions and perspectives for future research.

2 Edge states in Silicene

2.1 Silicene properties

Silicene, is a two-dimensional a monolayer honeycomb structure – like graphene, but with a slightly buckled geometry – of silicon, already synthesized [26, 27], in which has been attracting much interest due to its electronic structure, potential applications and its compatibility with silicon-based electronic technology, which dominates most nanotechnology today. Like graphene, in the absence of spin-orbit coupling (SOC), silicene has Dirac cones that cross the Fermi level at points $\boldsymbol{K}$ and $\boldsymbol{K}'$ [28, 29].

Another property present in both silicene and graphene is the quantum spin Hall effect (QSHE), a quantum state with non-trivial topological properties, characterized by the appearance of metallic edge state at the gap [30, 31], Initially, the QSHE was proposed by Kane and Mele for graphene, in which they stated that the precense of the SOC opens a band gap at the Dirac points [32]. However, it was later confirmed that the SOC in graphene is very weak, so that the QSHE in graphene can only occur at an unrealistically low temperature [33]. The QSHE was only observed for the first time in HgTe-CdTe quantum wells [34]. The problem was not solved yet, due its toxicity, difficulty in processing, and incompatibility with current silicon-based electronic technology, the HgTe-CdTe quantum wells become very unpractical. Silicene, however, has a relatively large SOC giving rise to bulk-gapped phases with metallic helical edge states (spin-momentum locked) and a band gap of 1.55 meV, thus leading the QSHE being more experimentally accessible.

2.1.1 Hamiltonian model

The buckled structure of a monolayer honeycomb structure is composed of two triangular sublattice, called A and B, as shown in Fig. 1. The noninteracting tight binding Hamiltonian H_{band} discribing a two-dimensional topological insulator structure for silicene, germanene, and stanene is:

$$H_{\text{band}} = -t \sum_{\langle i,j\rangle\sigma} c^{\dagger}_{i\sigma} c_{j\sigma} + \mathrm{i}\frac{\lambda_{\text{SO}}}{3\sqrt{3}} \sum_{\langle\langle i,j\rangle\rangle\sigma} \sigma \nu_{ij} c^{\dagger}_{i\sigma} c_{j\sigma} \tag{2.1}$$

where $c^{\dagger}_{i\sigma}$ ($c_{i\sigma}$) creates (annihilates) am electron in site i with spin orientation σ (here, when σ stands for $\sigma = \uparrow, \downarrow$ when used as a sub-index and for $\sigma = \pm 1$ when used within equations). In addition, $\langle i, j\rangle$ means that the sum runs over the nearest-neighbor site, while $\langle\langle i, j\rangle\rangle$ runs over the next-nearest-neighbor. The first term describes the nearest hoppings of a monolayer honeycomb lattice with transfer integral t. The second term the

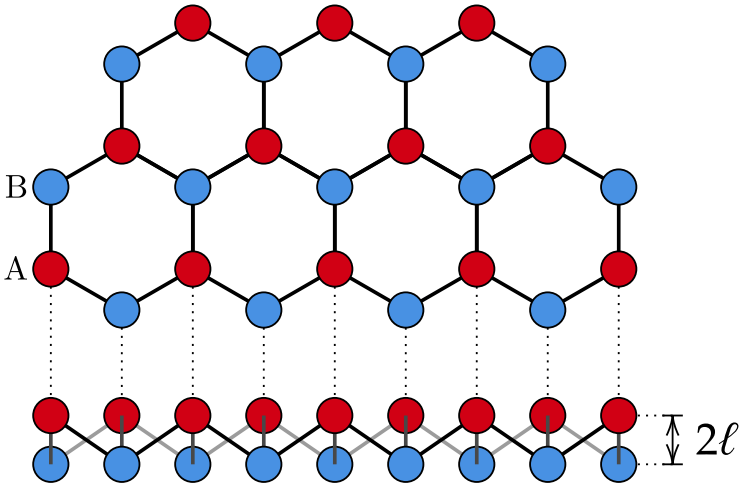

Figure 1 – Buckled honeycomb lattice of silicene, germanene or stanene. The lattice is built by two triangular sublattices, A and B, separated by a perpendicular distante 2ℓ.

	t (eV)	v_F	a (Å)	λ_{SO}
Graphene	2.8	9.8	2.46	10^{-3}
Silicene	1.6	1.6	3.86	3.9
Germanene	1.3	1.3	4.02	43
Stanene	1.3	1.3	4.70	100

Table 1 – Comparison between parameters characterizing graphene, silicene, germanene, and stanene. v_F is the Fermi velocity in units of 1×10^5 m/s, λ_{SO} and λ_{R} (Rashba SOC) in meV. θ is the bond angle. Adapted from Ref. [35].

effective spin-orbit interaction with coupling λ_{SO}, and $\nu_{ij}=+1$ if the next-nearest-neighbor hopping is counterclockwise and $\nu_{ij}=-1$ if it is clockwise (in relation to the positive z axis). In the Table 1 is showed some parameters values for silicene, germanene, and stanene, along with the graphene parameter for comparison. We can note that due the absent of buckled structure in graphene, his λ_{SO} is very small; thus, it is gapless and has no measurable topological properties. In Tables 1 it is also showed the Rashba spin-orbit interaction for each material, in which will be omitted in the calculation of this work. The λ_{SO} values in the Table 1 are all in units of t.

In order to discuss the effect of adding an magnetic impurity in a ribbon, we can add to the Hamiltonian (2.1) one term representing the impurity and another representing the hybridization between the ribbon and the impurity. It leads to total Hamiltonian $H=H_{\mathrm{band}}+H_{\mathrm{imp}}+H_{\mathrm{hyb}}$, where

$$H_{\mathrm{imp}}=\varepsilon_0(n_{\mathrm{imp},\uparrow}+n_{\mathrm{imp},\downarrow})+Un_{\mathrm{imp},\uparrow}n_{\mathrm{imp},\downarrow}, \tag{2.2}$$

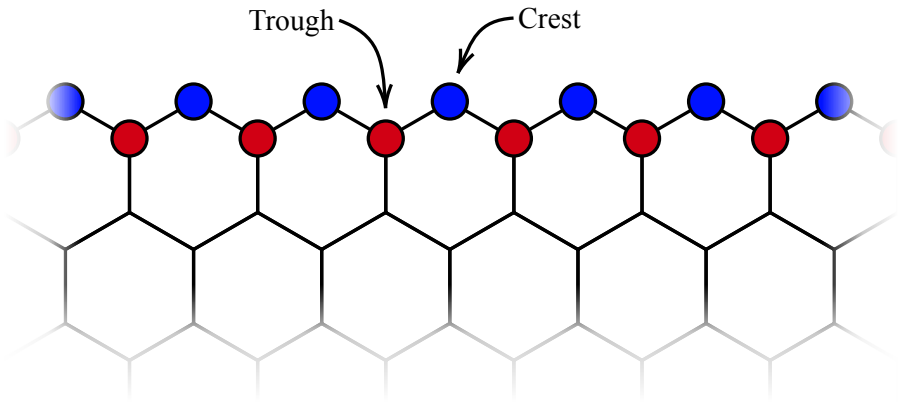

Figure 2 – Definition of the crest and through edges. The crest (blue circles) are the ones furthest from the edge, literally at the crest of the zigzag, while the trough (red circles) are the ones furthest inside the edge, at the valley of the edge.

$$H_{\text{hyb}} = V \sum_{\sigma} \left(c^{\dagger}_{\text{imp},\sigma} c_{k,\sigma} + \text{H.c.} \right), \tag{2.3}$$

where $n_{\text{imp},\sigma} = c^{\dagger}_{\text{imp},\sigma} c_{\text{imp},\sigma}$ and $c^{\dagger}_{\text{imp},\sigma}$ ($c_{\text{imp},\sigma}$) creates (annihilates) an electron at the impurity, which is described by a single-impurity Anderson model with Coulomb interaction U and orbital energy ε_0 (see Se. 3.1.1). A work form 2017 showed some results of effect of electron correlation in the presence of substitutional impurity (which replaces an atom from either sublattice and therefore has overlap integrals with more than one lattice site), which some results will presented in this section [1]. In this work was analyzed the effect of putting an impurity at the zigzag edge of a nanoribbon, in which has alternation of between site A and B, that will be refereed as "trough" and "crest" sites, respectively, henceforth (see Fig. 2). These results showed that the metallic topologically nontrivial states that screen the magnetic impurity reside in the crest sites, while the trough sites and their immediate neighborhood, as our spin correlation results have shown, behave as small metallic "puddles", which leak from the metallic edges and are surrounded by the bulk.

2.2 Zigzag nanoribbon and edge states

2.2.1 Band structure

A zigzag nanoriboon (ZNRB), as showed in Fig. 3, is characterized by containing only one type (A or B) of carbon atoms at the edge, which leads to formation of localized edge states near the Fermi level. The band structure of a ZNRB with periodic boundary conditions (PBCs) applied to the x direction and open boundary conditions (OBCs) applied in the y direction was shown in Fig. 4. The scpectrum is particle-hole symmetric around $E = 0$ and the energy levels for opposite momenta (k_x and $-k_x$) are mirrored

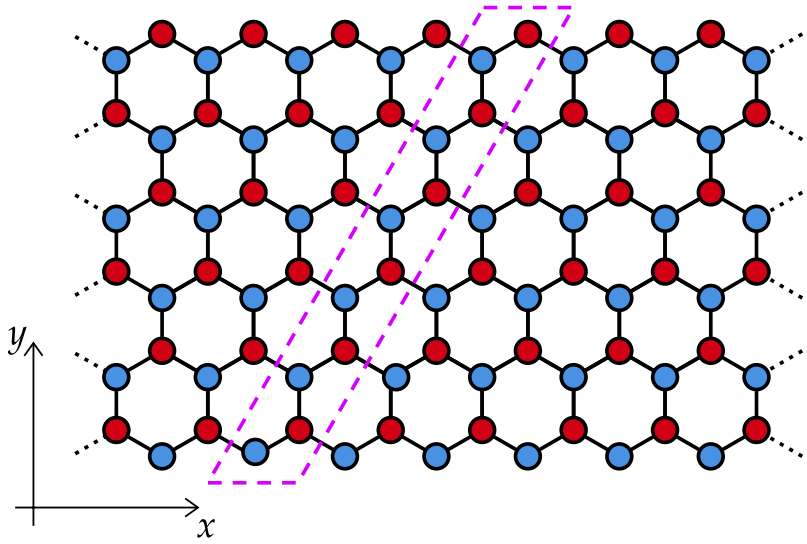

Figure 3 – Structure of ZNRB, a honeycomb lattice with zigzag open boundary condition. The dashed purple paralelogram represents the unit cell.

(Kramers degeneracy). A close-up of a specific region of the band structure – dashed red box in Fig. 4(a) – is shown. focusing on the bands that cross between the valence and conduction bands. These bands host the four helical edge states (two in each edge). Another close-up of the same region is shown in Fig. 4(c), but for a $\lambda_{SO} = 0.0$, (like graphene). This highlights the well-known flat bands associated with the edge states in graphene ZNRB [36].

Finally, in Fig. 4(d) is showed plot of the coefficient squared for each site across the ZNRB for the four edge states that are located symmetrically around $k_X = \pi$ ($k_{x1} = \pi - \delta$ and $k_{x2} = \pi + \delta = -k_{x1}$). Also , we have that k_{x1} and k_{x2} are time-reversed, indicating propagation in opposite directions.

We can not discuss so much on the effects of electronic interactions, since these are too weak to introduce noticeable spin correlations in the bulk, especially due to the vanishing density of states at the Dirac points.

2.2.2 Zigzag nanoribbon local density of states

The Fig. 5(a) shows the local density of states (LDOS) for the crest and through sites as the edge of the ZNRB. In this figure, we can check that the conducting edge states with spectral density at the Fermi energy ($\varepsilon_F = 0$) are mostly located at crest sites. Fig. 5(b) shows a contour plot of the LDOS for all sites in the OBC direction. The spectral density at the Fermi energy is restricted to the edge, and the other sites, therefore, occupie an insulating spectra, where the size of the gap partially derives from the spin-orbit coupling and from the confinement along the OBC direction. In Fig. 6, is shown a more detailed view, with increased resolution of the through LDOS, where we

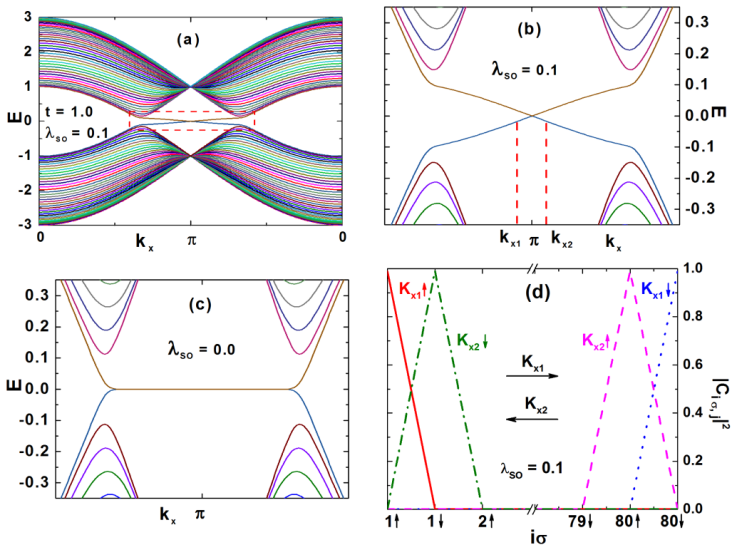

Figure 4 – (a) The energy spectra of a zigzag stanene nanoribbon for $\lambda_{SO} = 0.1$. (b) Close-up of the red dashed square in (a) showing details of the energy dispersion of the edge states. (c) Similar to (b), but for $\lambda_{SO} = 0.0$, which is appropriate for graphene. (d) Value of $|C_{i\sigma}|^2$ for the four metallic edge states associated with the wave vectors k_{x1} and k_{x2} in (b). Note that, as discussed in more detail in the text, they are located exclusively at crest sites, and states with different spin polarizations propagate in opposite directions at each edge. Figure adapted from Ref. [1]

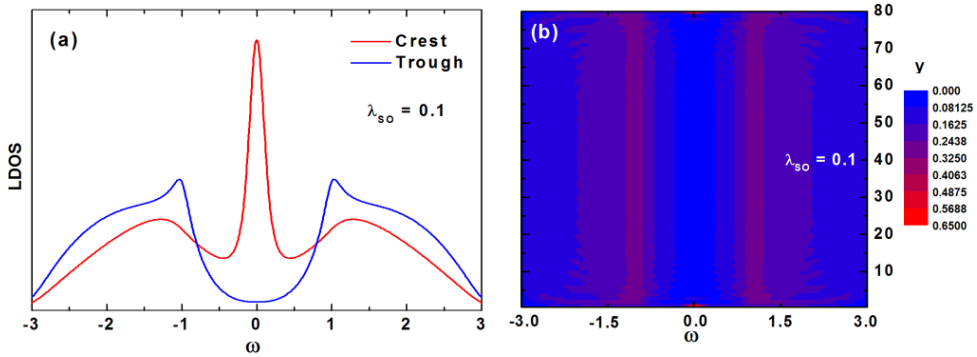

Figure 5 – (a) LDOS for two edge sites in the TI phase ($\lambda_{SO} = 0.1$): the crest site LDOS (red curve) displays a pronounced spectral density peak at the Fermi energy, while the trough site LDOS (blue curve) has very small, but finite, spectral density at the Fermi energy. (b) Color contour plot showing the LDOS across the width of a nanoribbon N = 80 sites wide ($\lambda_{SO} = 0.1$). Notice how the spectral density at the Fermi energy is located mostly at the edges [and primarily at crest sites, as shown in (a)], while the bulk remains gapped. Figure adapted from Ref. [1]

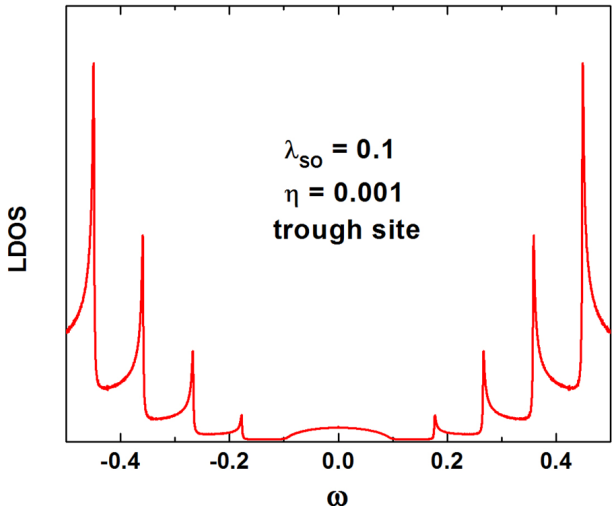

Figure 6 – Detail of the LDOS at a trough site, using a large number of poles and a small broadening $\eta = 0.001$ of the Green's function imaginary part. The spectral weight in the pesudogaplike region around the Fermi level is small but finite. Figure adapted from Ref. [1]

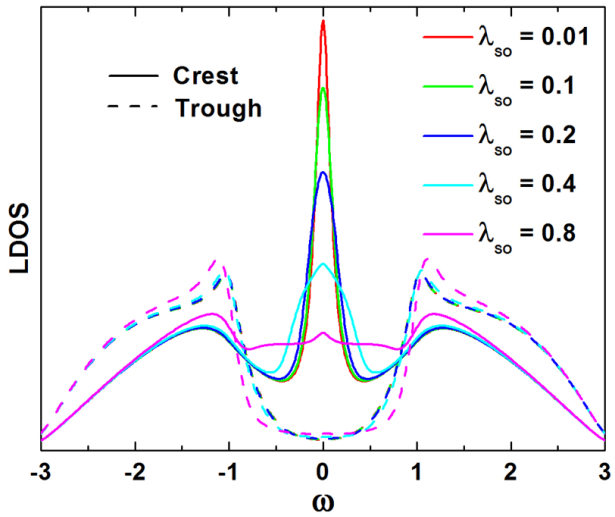

Figure 7 – Variation of the LDOS with the value of λ_{SO} for a crest site (solid lines) and a trough site (dashed lines). By varying λ_{SO} by almost two orders of magnitude, from 10×10^2 (most pronounced peak at $\omega = 0$) to 0.8 (almost flat at $\omega = 0$), we see that the main change in the LDOS of a crest site is the continuous spread of the spectral weight (located at the Fermi energy peak) into an almost flat distribution that covers the gap. The LDOS of a trough site almost does not vary with λ_{SO}. Figure adapted from Ref. [1]

can see the presence of a small, bu finite LDOS at the Fermi energy, and consequently the possibility for the formation of the Kondo state.

In Fig. 7 we can observe how the LDOS varies with SO coupling. This results shows that the only effect in the through site is a slight increase in the LDOS at the edge of the gap and a slight increase in the gap itself.

3 Kondo effect

3.1 Strong Correlated Electrons and Local Moments

Strong correlated systems are many-body states which the Coulombian interaction energy between electrons dominates the kinect energies. These systems are materials with d- or f-orbitals. These orbitals are heavily localized near the nucleus and this situation leads to a strong electronic repulsion between electrons in the same orbital. In the case where this orbitals are partially filled, can result in permanent magnetic moments.

The d- and f-orbitals can be ordered from the most localized from the last localized as [37]:

$$4f > 5f > 3d > 4d > 5d$$

. This leads to two trends: first, orbitals with larger principal quantum number n have more radial nodes and are more delocalized, and thus $5f < 4f$ and $5d < 4d < 3d$. Second, as the nuclear charge increases, the orbitals are pulled toward the nucleus, so that $nf > nd$.

In order to understand how electrons become concentrated and form magnetic properties in heavy-electron materials, we need to know how these localized magnetic moments interact with the Fermi sea within the material. As an example, consider an unpaired electron attached to an individual atom or ion, whose magnetic moment is described as

$$\boldsymbol{\mu} = -g_0\mu_B\boldsymbol{s} = \mu_B\boldsymbol{\sigma}, \tag{3.1}$$

where $2\boldsymbol{s} = \boldsymbol{\sigma} = (\sigma_x, \sigma_y, \sigma_z)$ is the Pauli matrices vector, $\mu_B = e\hbar/2m$ is the Bohr magnetom and g_0 is the gyromagnetic factor, which for non-relativistic electrons can be taken as $g_0 = 2$. The Hamiltonian describing systems in low-energy regime can be written as

$$H = -\boldsymbol{\mu} \cdot \boldsymbol{H} = -\mu_B\boldsymbol{\sigma} \cdot \boldsymbol{H}. \tag{3.2}$$

3.1.1 Anderson Impurity Model

The Anderson model of magnetic impurities is a model proposed in 1961 by Anderson [38] that can be used to describe magnetic impurities embedded in metals such as $3d$-bands of f-bands in rare-earth metals. In this model it is noticeable that moment formation has origins in strong Coulomb interactions, in which Coulomb repulsion, specially onsite between antiparallel spins, tends to localize electrons. Another feature noted by Anderson is the formation of an electronic resonance, in which an electron are amenable to tunneling between d- or f-orbitals and the conduction sea when their atomic energy level overlaps with the free electron band. [39, 37].

The Anderson Hamiltonian that depicts a model of localized moments orbital represented by field operators d_σ, $d_\sigma^\dagger$ (for $\sigma = \{\uparrow, \downarrow\}$), energy ε_d and Coulomb repulsion U is written as

$$H = \sum_{\boldsymbol{k},\sigma} \varepsilon_{\boldsymbol{k}\sigma} c_{\boldsymbol{k}\sigma}^\dagger c_{\boldsymbol{k}\sigma} + \varepsilon_d (n_{d\uparrow} + n_{d\downarrow}) + \sum_{\boldsymbol{k},\sigma} \left[V_{\boldsymbol{k}} c_{\boldsymbol{k}\sigma}^\dagger d_\sigma + V_{\boldsymbol{k}}^* d_\sigma^\dagger c_{\boldsymbol{k}\sigma} \right] + U n_{d\uparrow} n_{d\downarrow}. \tag{3.3}$$

where $c_{\boldsymbol{k}\sigma}$, $c_{\boldsymbol{k}\sigma}^\dagger$ are field operator of the conduction band electrons with momentum $\boldsymbol{k}$, spin σ, and energy $\varepsilon_{\boldsymbol{k}\sigma} = E_{\boldsymbol{k}\sigma} - \mu$.

3.1.2 Virtual Bound Formation and Non-Interacting Resonance

In order to illustrate some properties of the Anderson model, we will first turn off the interaction U, considering only the hybridization effects. We can examine the behavior of the d/f-orbitals through Green's Function and equation of motion.

The retarded Green's function of the localized states is defined as:

$$G_{d\sigma}(t - t') = -i\theta(t - t') \left\langle \left\{ d_\sigma(t), d_\sigma^\dagger(t') \right\} \right\rangle. \tag{3.4}$$

We can write the equation of motion by taking the derivative in t in Green's function (3.4), which gives us

$$\begin{aligned} \mathrm{i}\partial_t G_{d\sigma}(t - t') &= -\mathrm{i}[\mathrm{i}\partial_t \theta(t - t')] \left\langle \left\{ d_\sigma(t), d_\sigma^\dagger(t') \right\} \right\rangle - \mathrm{i}\theta(t - t') \left\langle \left\{ \mathrm{i}\partial_t d_\sigma(t), d_\sigma^\dagger(t') \right\} \right\rangle \\ &= \delta(t - t') + \mathrm{i}\theta(t - t') \left\langle \left\{ [H, d_\sigma(t)], d_\sigma^\dagger(t') \right\} \right\rangle. \end{aligned} \tag{3.5}$$

Developing the commutator in the above equation and doing some manipulations, we can rewrite it in terms of the Green's function $G_{\boldsymbol{k}d\sigma}$:

$$G_{\boldsymbol{k}d\sigma}(t - t') = \mathrm{i}\theta(t - t') \left\langle \left\{ c_{\boldsymbol{k}\sigma}(t), d_\sigma^\dagger(t') \right\} \right\rangle, \tag{3.6}$$

in which the Eq. (3.5) is rewritten as

$$(\mathrm{i}\partial_t - \varepsilon_d) G_{d\sigma} = \delta(t - t') + \sum_{\boldsymbol{k}} V_{\boldsymbol{k}} G_{\boldsymbol{k}d\sigma}. \tag{3.7}$$

We can also write the equation of motion for the Green's function (3.6), which gives

$$(\mathrm{i}\partial_t - \varepsilon_{\boldsymbol{k}}) G_{\boldsymbol{k}d\sigma} = V G_d. \tag{3.8}$$

Taken the Fourier transform of both Eq. (3.7) and (3.8) give us a system of coupled equations

$$(\omega - \varepsilon_d) G_{d\sigma}(\omega) - \sum_{\boldsymbol{k}} V_{\boldsymbol{k}} G_{\boldsymbol{k}d\sigma}(\omega) = 1, \tag{3.9}$$

$$(\omega - \varepsilon_{\boldsymbol{k}}) G_{\boldsymbol{k}d\sigma}(\omega) - V_{\boldsymbol{k}} G_{d\sigma}(\omega) = 0, \tag{3.10}$$

where to ensure the convergence of the Fourier transform, the frequency ω can be added to a infinitesimal imaginary term as $\omega \to \omega + i\eta$.

We can use the fact that $[G^0_{\boldsymbol{k}\sigma}(\omega)]^{-1} = \omega - \varepsilon_{\boldsymbol{k}}$ and write Eq. (3.10) in the form

$$G_{\boldsymbol{k}d\sigma}(\omega) = G^0_{\boldsymbol{k}\sigma}(\omega) V_{\boldsymbol{k}} G_{d\sigma}(\omega), \tag{3.11}$$

and inserting in the (3.9) we get

$$G_{d\sigma}(\omega) = G^0_{\boldsymbol{k}\sigma}(\omega) + G^0_{\boldsymbol{k}\sigma}(\omega)\Sigma_\sigma(\boldsymbol{k},\omega) G_{d\sigma}(\omega), \tag{3.12}$$

where $\Sigma_\sigma(\boldsymbol{k},\omega)$ is called *self-energy* and is defined as

$$\Sigma_\sigma(\boldsymbol{k},\omega) = \sum_{\boldsymbol{k}} |V_{\boldsymbol{k}}|^2 G^0_{\boldsymbol{k}\sigma}(\omega) = \sum_{\boldsymbol{k}} \frac{|V_{\boldsymbol{k}}|^2}{\omega - \varepsilon_{\boldsymbol{k}}}. \tag{3.13}$$

Solving the Eq. (3.12), we got

$$G_{d\sigma}(\omega) = \frac{1}{[G^0_{d\sigma}(\omega)]^{-1} + \Sigma_\sigma(\boldsymbol{k},\omega)} = \frac{1}{\omega + \mathrm{i}\eta - \varepsilon_d + \Sigma_\sigma(\boldsymbol{k},\omega)}. \tag{3.14}$$

Now considering a broad conduction band and that the coupling $V_{\boldsymbol{k}}$ depends only on $k = |\boldsymbol{k}|$, we can approximate the self-energy as an integral, so that

$$\Sigma_\sigma(k,\omega) = \int \frac{\mathrm{d}\varepsilon}{\pi} \rho(\varepsilon) \frac{\pi V_k^2}{\omega + \mathrm{i}\eta - \varepsilon} = \int \frac{\mathrm{d}\varepsilon}{\pi} \frac{\Delta(\varepsilon)}{\omega + \mathrm{i}\eta - \varepsilon}, \tag{3.15}$$

where $\rho(\varepsilon)$ is the density of states of the conduction band, and $\Delta = \pi\rho(\varepsilon)V_k^2$. For simplicity we will assume a uniform density of state and thus a contant $\Delta(\varepsilon) = \Delta$. Lets assume too that the chemical potential lies in the middle of gap and a broad conduction band of width $[-D, D]$. So we have

$$\Sigma_\sigma(k,\omega) = \frac{\Delta}{\pi} \int_D^D \mathrm{d}\varepsilon \, \frac{1}{\omega + \mathrm{i}\eta - \varepsilon} = \log\left[\frac{\omega + \mathrm{i}\eta + D}{\omega + \mathrm{i}\eta - D}\right]. \tag{3.16}$$

In order to simplify the above equation, we can use the *Cauchy principal values* which states that

$$\log(x \pm \mathrm{i}\eta) = \log|x| + \mathrm{i}\pi\theta(-x) = \begin{cases} \log|x|, & x > 0, \\ \log|x| \pm \mathrm{i}\pi, & x < 0. \end{cases} \tag{3.17}$$

So the Eq. (3.16) becomes

$$\begin{aligned} \Sigma_\sigma(k,\omega) &= \frac{\Delta}{\pi}\{\log(\omega \pm \mathrm{i}\eta + D) - \log(\omega \pm \mathrm{i}\eta - D)\} \\ &= \frac{\Delta}{\pi}\{\log|\omega + D| - \log|\omega - D| \pm \mathrm{i}\pi\theta(-\omega - D) \mp \mathrm{i}\pi\theta(-\omega + D)\} \\ &= \frac{\Delta}{\pi} \log\left|\frac{\omega + D}{\omega - D}\right| \mp \mathrm{i}\Delta\theta(D - |\omega|). \end{aligned} \tag{3.18}$$

We can see that for a broad band where $\omega \ll D$ we have that $\log|(\omega+D)/(\omega-D)| \approx |\omega/D|$ is negligible. So the f-propagator becomes

$$G_{d\sigma} = \frac{1}{\omega + \mathrm{i}\eta - \varepsilon_d - \mathrm{i}\Delta}, \tag{3.19}$$

which describes a resonance with a width Δ, centered around energy ε_d. The density of states can be obtained as

$$\rho_{d\sigma}(\omega) = \frac{1}{\pi}\operatorname{Im} G_{d\sigma}(\omega) = \frac{\Delta}{(\omega-\varepsilon_d)^2 + \Delta^2}. \tag{3.20}$$

3.1.3 Full Anderson Model

Now we will loot at the full Anderson model, that is the case where we have $U \neq 0$. For this situation the equation of motion for $G_{d\sigma}(t-t')$ become

$$\begin{aligned}\mathrm{i}\partial_t G_{d\sigma} &= \delta(t-t') - \mathrm{i}\theta(t-t')\left\langle\left\{[d_\sigma(t), H], d_\sigma^\dagger(t')\right\}\right\rangle \\ &= \delta(t-t') + \varepsilon_d G_{d\sigma} + V\sum_{\boldsymbol{k}} G_{\boldsymbol{k}d\sigma} - i\theta(t-t')U\left\langle\left\{d_\sigma(t)n_{\sigma'}, d_\sigma^\dagger(t')\right\}\right\rangle.\end{aligned} \tag{3.21}$$

And for $G_{\boldsymbol{k}d\sigma}(t-t')$,

$$\begin{aligned}\mathrm{i}\partial_t G_{\boldsymbol{k}d\sigma} &= \delta(t-t') - \mathrm{i}\theta(t-t')\left\langle\left\{[c_{\boldsymbol{k}\sigma}(t), H], d_\sigma^\dagger(t')\right\}\right\rangle \\ &= \varepsilon_{\boldsymbol{k}\sigma} G_{\boldsymbol{k}d\sigma} - V_{\boldsymbol{k}} G_{d\sigma}.\end{aligned} \tag{3.22}$$

The set of equations (3.21) and (3.22) does not close. To overcome this problem we can made use of the *mean field approximation*, in which the interaction term of the Hamiltonian can be approximated as

$$Un_\uparrow n_\downarrow = Un_\uparrow\langle n_\downarrow\rangle + U\langle n_\uparrow\rangle n_\downarrow - U\langle n_\uparrow\rangle\langle n_\downarrow\rangle + \mathcal{O}(\delta n^2). \tag{3.23}$$

Without loss of generation, we will consider here $\sigma = \uparrow$. Using the mean field approximation, the last term of Eq. (3.21) will become

$$\begin{aligned}-i\theta(t-t')U\left\langle\left\{d_\uparrow(t)n_\downarrow, d_\uparrow^\dagger(t')\right\}\right\rangle &= -i\theta(t-t')U\langle n_\downarrow\rangle\left\langle\left\{d_\uparrow(t), d_\uparrow^\dagger(t')\right\}\right\rangle \\ &= \langle n_\downarrow\rangle G_{d\uparrow},\end{aligned} \tag{3.24}$$

and taken the Fourier transform of Eq. (3.21) and Eq. (3.22), we will get the following set of equations:

$$(\omega - \varepsilon_d - U\langle n_\downarrow\rangle)G_{d\uparrow}(\omega) - \sum_{\boldsymbol{k}} V_{\boldsymbol{k}} G_{\boldsymbol{k}d\uparrow}(\omega) = 1, \tag{3.25}$$

$$(\omega - \varepsilon_{\boldsymbol{k}\uparrow})G_{\boldsymbol{k}\uparrow}(\omega) - V_{\boldsymbol{k}} G_{d\uparrow}(\omega) = 0. \tag{3.26}$$

Solving again, for general spin orientation, we get $G_{d\sigma}$ as

$$G_{d\sigma}(\omega) = \frac{1}{\omega + \mathrm{i}\eta - \varepsilon_d - U\left\langle n_{\bar{\sigma}}\right\rangle + \Sigma_\sigma(\boldsymbol{k}, \omega)}, \tag{3.27}$$

where $\bar{\sigma}$ represents the opposite spin orientation of σ. Now we can obtain the spectral function, defined as

$$\begin{aligned} A_{d\sigma}(\omega) &= -2\,\mathrm{Im}\, G_{d\sigma}(\omega) \\ &= \frac{\Delta}{\left(\omega + \mathrm{i}\eta - \varepsilon_d - U\left\langle n_{\bar{\sigma}}\right\rangle\right)^2 + \Delta^2}. \end{aligned} \tag{3.28}$$

The mean occupancy of a quantum state can be found in terms of the spectral function using the relation

$$\left\langle n_{d\sigma}\right\rangle = \int \frac{\mathrm{d}\omega}{2\pi} A_{d\sigma}(\omega) n_{\mathrm{F}}(\omega), \tag{3.29}$$

where $n_{\mathrm{F}}(\omega)$ is the Fermi-Dirac distribution, which at zero temperature can be taken as $n_{\mathrm{F}}(\omega) = \theta(-\omega)$. Solving this integral, for both spin-up and spin-down we get the following self-consistency equation

$$\left\langle n_{d\uparrow}\right\rangle = \frac{1}{2} - \frac{1}{\pi}\tan^{-1}\left(\frac{\varepsilon_d + U\left\langle n_{d\downarrow}\right\rangle}{\Delta}\right), \tag{3.30}$$

$$\left\langle n_{d\downarrow}\right\rangle = \frac{1}{2} - \frac{1}{\pi}\tan^{-1}\left(\frac{\varepsilon_d + U\left\langle n_{d\uparrow}\right\rangle}{\Delta}\right), \tag{3.31}$$

and using the relation $\cot[\pi/2 - \tan^{-1}(x)] = x$,

$$\cot(\pi\left\langle n_{d\sigma}\right\rangle) = \frac{\varepsilon_d + U\left\langle n_{d\bar{\sigma}}\right\rangle}{\Delta}, \tag{3.32}$$

and

$$\left\langle n_{d\sigma}\right\rangle = \frac{1}{\pi}\cot^{-1}\left(\frac{\varepsilon_d + U\left\langle n_{d\bar{\sigma}}\right\rangle}{\Delta}\right). \tag{3.33}$$

It is convenient to introduce the total occupancy $n = \left\langle n_{d\uparrow}\right\rangle + \left\langle n_{d\downarrow}\right\rangle$ and the total magnetization $M = \left\langle n_{d\uparrow}\right\rangle - \left\langle n_{d\downarrow}\right\rangle$, and combining both we can rewrite the occupancy of a quantum state as

$$\left\langle n_{d\sigma}\right\rangle = \frac{1}{2}(n + \sigma M) \tag{3.34}$$

where $\sigma = \pm 1$ for spin-up and spin-down. So the total occupancy and magnetization are then

$$n = \frac{1}{\pi}\sum_{\sigma=\pm 1}\cot^{-1}\left[\frac{\varepsilon_d + U(n - \sigma M)/2}{\Delta}\right], \tag{3.35}$$

$$M = \frac{1}{\pi}\sum_{\sigma=\pm 1}\sigma\cot^{-1}\left[\frac{\varepsilon_d + U(n - \sigma M)/2}{\Delta}\right]. \tag{3.36}$$

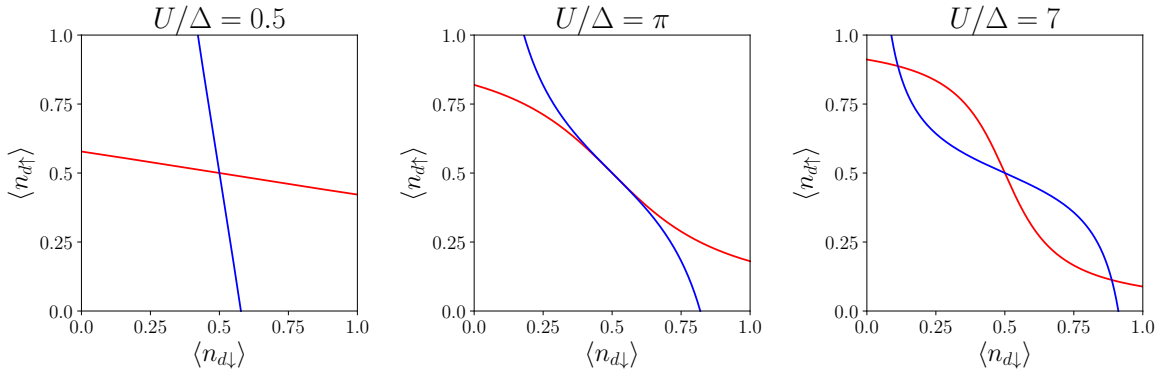

Figure 8 – Plot of the magnetization $\langle n_{d\uparrow} \rangle$ as function of $\langle n_{d\downarrow} \rangle$, using Eqs. (3.30) and (3.31). We can see that for $U/\Delta < \pi$ there's only solution with zero magnetization, while for $U/\Delta > \pi$, we can have a state without magnetization and two with a non-zero magnetization.

In order to find the critical values of the interaction $U - U_c$, where a local moment develops, we set $M \to 0^+$ in Eq. (3.35) for which we obtain

$$n = \frac{2}{\pi} \cot^{-1}\left(\frac{\varepsilon_d + Un/2}{\Delta}\right) \Longrightarrow \cot\left(\frac{\pi n}{2}\right) = \frac{\varepsilon_d + U_c n/2}{\Delta}, \tag{3.37}$$

and using the relation $\cot^{-1}(a + bx) = \cot^{-1}(a) - bx/(1 + a^2) + \mathcal{O}(x^2)$ we can linearize the left hand side of Eq. (3.36) to get

$$1 = \frac{U_c}{\pi\Delta} \frac{1}{1 + (\varepsilon_d + U_c n/2)^2 \Delta^2} = \frac{U_c}{\pi\Delta} \sin^2\left(\frac{\pi n}{2}\right), \tag{3.38}$$

Using the half-filling condition $\varepsilon_d = -U/2$ we get $n = 1$ and the following condition is obtained

$$U_c = \pi\Delta. \tag{3.39}$$

Fig 8 shows that for $U/\Delta > \pi$, the mean field Anderson model has three solution, being one without any magnetization and two with a net magnetization. $U/\Delta < \pi$ always produces a no magnetized states.

3.2 Kondo effect

Normally in pure metals like Au and Cu, the electrical resistance decrease as the temperatures is lowered until reach a saturation. This reduction of resistance can be understood as result of the small lattice vibration for low temperature, thus reducing the electronic inelastic scattering processes. Even at incredibly low temperatures, certain metals can still has a residual resistance. Their resistance reaches a steady, finite value, and this "saturation resistance" is influenced by the number of imperfections within the

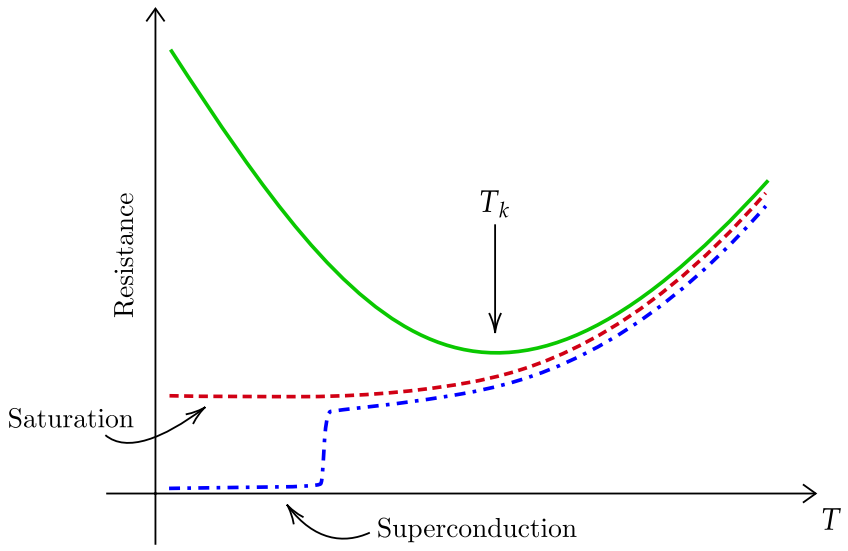

Figure 9 – Graphic representing the behavior resistance in three different regime. The red dotted line represents the expected behavior of the resistance for low temperatures where the resistance saturates. The blue dotted line represents the superconductive phase, where lower than a critical temperature the resistivity abruptly vanishes. Finally the green solid line represents the observed Kondo effect where the resistance decrease until a minimum value at some temperature T_K and starts to increase as lower the temperature.

material. The more defects there are, the higher this resistance becomes, although the character of the temperature dependence remains the same.

Certain metals, like Pb, Nb, and Al, after the temperature decreases to a critical temperature, they can suddenly loose all resistance and enter a superconducting state. This dramatic shift from a normal conducting state to a superconductor is a fascinating example of how the behavior of many electrons can be quite different from that of individual electrons.

However, adding impurity containing dilute magnetic moments, such as a low concentration of Mn or Fe in Cu, drastically changes the situation, where the resistance decreases until a minimum an the start to increases as the temperature continue to fall. This phenomenon was first explained by Kondo in 1964 [4], but the understanding of the ground state properties of this problem would only be solved later in 1980 through renormalization-group (RNG) approach [10, 11]. In Fig. 9 is showed the behavior of the resistivity under Kondo regime and a comparison between the normal and the superconductive case.

3.2.1 The Kondo Hamiltonian

In the last section, we provided a explanation of the formation of magnetic moment at magnetic impurity in nonmagnetic metallic hosts via mean field approximation to the Anderson impurity model. This model, however, fails to predict the low temperature

properties of the system, as example the disappearance of the moments at low temperatures. In order to describe this properties, Kondo proposed the following Hamiltonian

$$H_K = \sum_{\boldsymbol{k}\sigma} \varepsilon_{\boldsymbol{k}\sigma} c^\dagger_{\boldsymbol{k}\sigma} c_{\boldsymbol{k}\sigma} + J\boldsymbol{S}\cdot\boldsymbol{s}(0), \tag{3.40}$$

where $\boldsymbol{S}$ represent the local impurity moment, and $\boldsymbol{s}(0)$ is the spin density of the conduction electrons at the impurity site.

Now in order to determine the coefficient J we will discuss the the processes, in the Anderson model, that lead to scattering of a conduction electron with a local moment. As we have discussed in the last section, the mean field approximation in the Anderson model can rise when the localized energy level has less than the Fermi level, but the interaction strength is large enough that the energy to have two electrons is greater than the Fermi level, avoiding double occupancy. Using perturbation theory up to the second order, it is possible to calculate the hybridization interaction which couples conduction electrons to the local moment.

We can write the single occupied ground state as

$$\left|d^1_\sigma\right\rangle = d^\dagger_\sigma \prod_{|\boldsymbol{k}|\leq|\boldsymbol{k}_\mathrm{F}|} c^\dagger_{\boldsymbol{k}\uparrow} c^\dagger_{\boldsymbol{k}\downarrow} \left|0\right\rangle . \tag{3.41}$$

We will also define a double occupied excited state

$$\left|d^2\right\rangle = d^\dagger_{\bar\sigma} c_{\boldsymbol{k}\bar\sigma} \left|d^1_\sigma\right\rangle , \tag{3.42}$$

and an empty excited state

$$\left|d^0\right\rangle = c^\dagger_{\boldsymbol{k}\sigma} d_\sigma \left|d^1_\sigma\right\rangle . \tag{3.43}$$

Both excited states cost the same amount of energy $U/2$, so the system becomes electron–hole symmetric. The impurity can can switch its magnetization through either of two virtual processes, each with a transition rate $2V^2/U$ [39]:

$$\begin{aligned}\left|d^1_{\bar\sigma}\right\rangle &= c^\dagger_{\boldsymbol{k}'\sigma} d_\sigma \left|d^2\right\rangle \\ &= c^\dagger_{\boldsymbol{k}'\sigma} d_\sigma d^\dagger_{\bar\sigma} c_{\boldsymbol{k}\bar\sigma} \left|d^1_\sigma\right\rangle\end{aligned} \tag{3.44}$$

$$\begin{aligned}\left|d^1_{\bar\sigma}\right\rangle &= d^\dagger_{\bar\sigma} c^\dagger_{\boldsymbol{k}'\bar\sigma} \left|d^0\right\rangle \\ &= d^\dagger_{\bar\sigma} c^\dagger_{\boldsymbol{k}'\bar\sigma} c^\dagger_{\boldsymbol{k}\sigma} d_\sigma \left|d^1_\sigma\right\rangle .\end{aligned} \tag{3.45}$$

The processes (3.44) and (3.45) are respectively represented in the Fig. 10a and 10b.

Classically, one could say that these process are not possible because, the process where an electron in a single occupied state hops to the Fermi sea, would be forbidden since it would require a large amount of energy. But in quantum mechanics, due to the

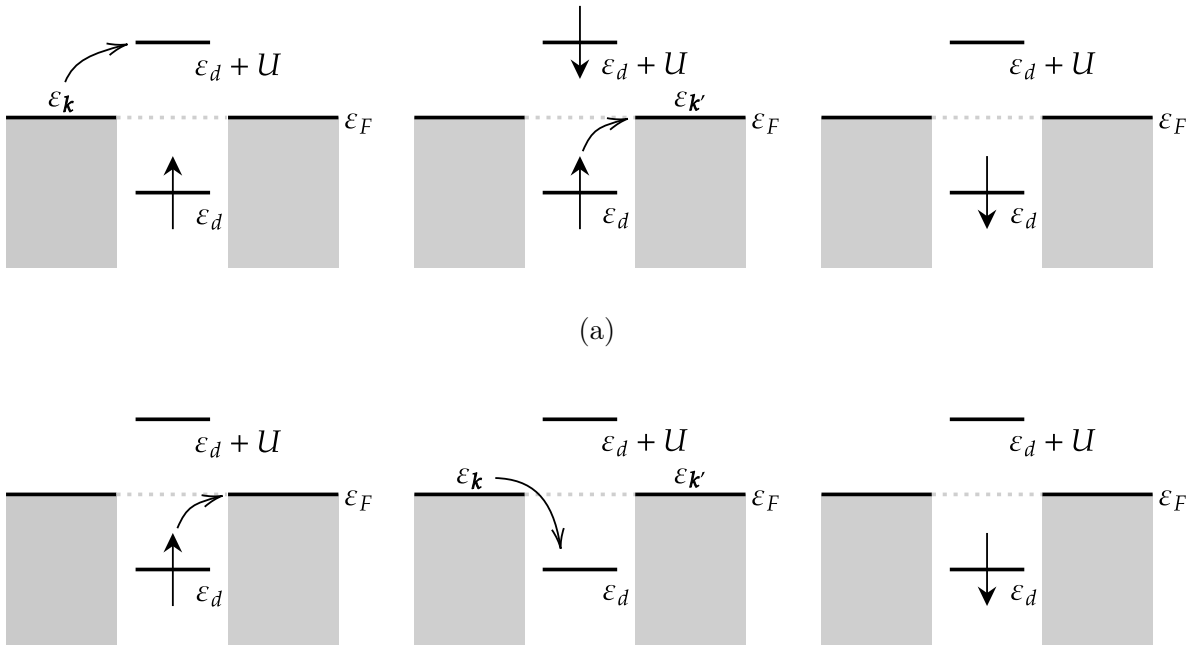

Figure 10 – Two different processes of spin flip for the Anderson model: (a) first a electron with momentum $\boldsymbol{k}$ with spin-↑ at the Fermi sea hops to the impurity site; the intermediate double occupied process with energy $2\varepsilon_d + U$; the electron with spin-↓ at the impurity hops to the Fermi sea with momentum $\boldsymbol{k}'$. (b) the electron at the impurity with spin-↑ hops to the Fermi sea with momentum $\boldsymbol{k}'$; then the electron with spin-↓ and momentum $\boldsymbol{k}$ at Fermi sea hops to the impurity.

Heisenberg uncertainty principle $\Delta\varepsilon\Delta t \geq \hbar/2$, this process is allowed for a very short time - around $\hbar/|\varepsilon_d|$. During this time interval, another electron must tunnel form the Fermi sea to the impurity; however, then spin orientation of this electron may be in opposite direction.

We can consider a regime where $\Delta \ll |\varepsilon_d|$, $\varepsilon_d \ll \varepsilon_\mathrm{F}$ – which we are using $\varepsilon_\mathrm{F} = 0$ – and $\varepsilon_d + U > 0$, the energies of the excited states $|d^0\rangle$ and $|d^2\rangle$ can be neglected at low temperatures, and thus a spin-1/2 moment is formed. As a result, at low temperature, the local charge fluctuations on the d-level are restricted. Consequently, only virtual interactions with electrons in the conduction band remain influential, leading to spin-flip processes.

The scattering amplitude of the spin-flip processes can be calculated using the perturbation theory. We get the scattering amplitude of such processes as [40]

$$T = \frac{V_{\boldsymbol{k}} V_{\boldsymbol{k}'}}{E_\mathrm{i} - E_\mathrm{int}}, \tag{3.46}$$

where E_i is the energy of the initial state and E_int is the energy of the intermediate state. Let us discuss two scattering processes. First, consider a process where the initial state is

a conduction electron in state $\boldsymbol{k}$ with spin-$\downarrow$ and an electron at the impurity with spin-$\uparrow$, scattered at a state made up of a conduction electron in state $\boldsymbol{k}' \uparrow$ and an impurity with spin-$\downarrow$. The processes can be done as follows: first the electron $\boldsymbol{k}$ hops, via the hybridization interaction, to the impurity. In this intermediate state, the impurity is double occupied, whose energy is $2\varepsilon_d + U$. Then the spin-$\downarrow$ electron at the impurity hops to the conduction band in state $\boldsymbol{k}'$. The scattering amplitude for this process in a general form is

$$T_{(\boldsymbol{k}\sigma)+(d\bar{\sigma})\longrightarrow(\boldsymbol{k}'\sigma)+(d\bar{\sigma})} = \frac{V_{\boldsymbol{k}}V_{\boldsymbol{k}'}}{\varepsilon_{\boldsymbol{k}} - \varepsilon_d - U}. \tag{3.47}$$

The second process is the scattering of a conduction electron in state $\boldsymbol{k}$ with spin-$\uparrow$ with a spin-$\uparrow$ to a final electron in state $\boldsymbol{k}' \uparrow$ and impurity remaining with spin-$\uparrow$. In the intermediate state, both electrons are in conduction states, whose scattering amplitude is

$$T_{(\boldsymbol{k}\sigma)+(d\sigma)\longrightarrow(\boldsymbol{k}'\sigma)+(d\sigma)} = -\frac{V_{\boldsymbol{k}}V_{\boldsymbol{k}'}}{\varepsilon_d - \varepsilon_{\boldsymbol{k}'}}, \tag{3.48}$$

where the minus size arises from the exchange between conduction electrons and electrons at impurity, as the initial conduction electron ends on the impurity and the initial electron at the impurity end up in the conduction band.

Now we can write the amplitude of the spin-flip process as a superposition of both individual process, which yields

$$T_{(\boldsymbol{k}\sigma)+(d\bar{\sigma})\longrightarrow(\boldsymbol{k}'\bar{\sigma})+(d\sigma)} = -V_{\boldsymbol{k}}V_{\boldsymbol{k}'}\left(\frac{1}{\varepsilon_{\boldsymbol{k}} - \varepsilon_d - U} + \frac{1}{\varepsilon_d - \varepsilon_{\boldsymbol{k}'}}\right), \tag{3.49}$$

where again the minus sign again comes from the exchange of the conduction and impurity electrons.

Similarly, the amplitude for the spin-flip process can be calculated using the Kondo model, in which the result is:

$$T_{(\boldsymbol{k}\sigma)+(d\bar{\sigma})\longrightarrow(\boldsymbol{k}'\bar{\sigma})+(d\sigma)} = -\frac{1}{2}.J \tag{3.50}$$

Comparing the Eqs. (3.49) and (3.50), we get

$$J = 2V_{\boldsymbol{k}}V_{\boldsymbol{k}'}\left(\frac{1}{\varepsilon_{\boldsymbol{k}} - \varepsilon_d - U} + \frac{1}{\varepsilon_d - \varepsilon_{\boldsymbol{k}'}}\right). \tag{3.51}$$

As we are dealing with $\boldsymbol{k}$-states near close to the Fermi level, we can chose $\varepsilon_{\boldsymbol{k}} \approx \varepsilon_{\boldsymbol{k}'} \approx 0$, and thus, the above equation becomes

$$J = -|V_{\boldsymbol{k}}|^2 \frac{U}{|\varepsilon_d|(U - |\varepsilon_d|)} < 0. \tag{3.52}$$

The above result shows that the interaction strength between the d-orbital impurity and the sea of electrons exhibits antiferromagnetic character. To determine its magnitude,

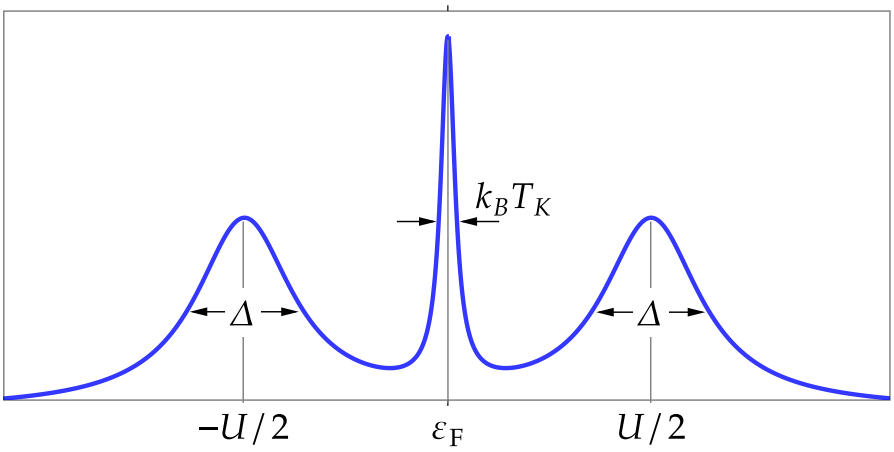

Figure 11 – Density of states for the singlet ground-state, where the excess of density of states in the conduction band appears as a Kondo resonance at the Fermi level.

we focus on the condition where the d-level energy satisfy a particle-hole symmetry, i.e., $\varepsilon_d - U/2$. In this configuration, the exchange interaction becomes

$$J = -4\frac{|V_{\boldsymbol{k}}|^2}{U}, \tag{3.53}$$

in which it can be verified that the exchange interaction is inversely proportional to the on-site Coulomb repulsion. Thus, the Kondo interaction in the Anderson model is mediated by the charge fluctuations between the conduction band and the impurity level.

The equivalence between the Anderson and Kondo models can be achieved, by means of the Schrieffer-Wolff transformation [37, 39]. This equivalence leads us to infer that both model share the same singlet ground state. At first, we are tempted to suggest that the formation of a singlet state in the Anderson model would occur due to double occupancy of the impurity levels. However, as we discussed earlier, the double occupied impurity level lie high above the Fermi level and therefore unoccupied. In fact the singlet state comes from a new resonant level arising from the spin exchange between the Fermi sea and the impurity level. When many such processes are taken together, this results in the d-level being nearly singly occupied, but not quite. This excess of electron density of states occupies the conduction band, and due to the Pauli exclusion principle, this small amount of density of state appears at the Fermi level, giving a rise of *Kondo resonance*, as shown in Fig. 11.

3.3 RKKY interaction

In the last section we discussed the mechanism of the formation of antiferromagnetic order at low temperatures by local magnetic moment metals in a nonmagnetic metal host.

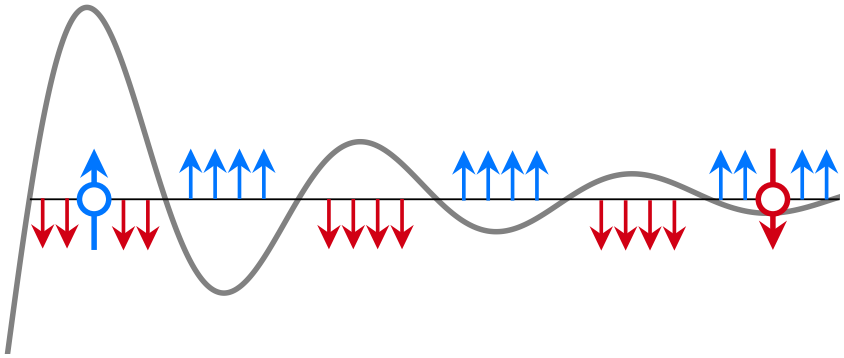

Figure 12 – Illustration of the oscillation in the spin polarization around a magnetic impurity, giving rise to the RKKY interaction.

It is known that when a charge is added in the Fermi sea, the electronic density of state will change to shield this charge, developing the so-called *Friedel oscillations* [41, 17]. How if this charge has a net magnetic moment, this will also induce a changing in the electronic density of state. This give rise of a situation in which the magnetic nature of a system is associated with itinerant conduction electrons, leading to indirect exchange processes mediated by the spin polarization of conduction electrons. This mechanism is known as Ruderman-Kittel-Kasuya-Yosida (RKKY) interaction [15, 16, 42], and is schematically represented in Fig. 12. This mechanism is normally calculated through second-order perturbation theory with respect to exchange interaction between the magnetic impurity and the conduction electrons of the metal host.

We can derive the effective Hamiltonian at finite temperature. Let us consider a Hamiltonian with a contact exchange interaction between the local moment and the host electrons as

$$H = H_0 + V, \tag{3.54}$$

where H_0 is the non-interacting Hamiltonian of the electron system. V is the interactive part of the Hamiltonian, which will be treated as a perturbation, defined as

$$V = -J(\boldsymbol{S}_i \cdot \boldsymbol{s}_i + \boldsymbol{S}_j \cdot \boldsymbol{s}_j), \tag{3.55}$$

where, as like the Eq. (3.40), $\boldsymbol{S}_i$ represent the local impurity moment, and $\boldsymbol{s}_i$ is the spin density of the conduction electrons at the impurity site.

Here we present a derivation based on Ref. [43]. First, consider the thermodynamic potential Ω defined as

$$\exp(-\beta\Omega) = \mathrm{Tr}\{\exp(\beta H_0)S(\beta)\}, \tag{3.56}$$

where $S(\beta)$ is defined as

$$S(\beta) = T_\tau \exp\left\{-\int_0^\beta \mathrm{d}\tau\, V(\tau)\right\}, \tag{3.57}$$

being $\tau = it$ the imaginary time and T_τ the time ordering operator. The goal is to compute ω until second order perturbation. For this is more convenient to rewrite the Eq. (3.56) by terms of the S-matrix expansion [41]:

$$\exp(-\beta\Omega) = \exp(-\beta\Omega_0)\sum_{n=0}^{\infty}\frac{(-1)^n}{n!}\int_0^\beta \mathrm{d}\tau_1\cdots\int_0^\beta \mathrm{d}\tau_n \left\langle T_\tau \hat{V}(\tau_1)\cdots\hat{V}(\tau_n)\right\rangle, \tag{3.58}$$

where Ω_0 is the value of Ω in the limit of vanishing interaction, and the "hat" at the $\hat{V}$'s means that it is in the interaction picture [37, 41, 39], and thus the expectation value above must be evaluated in the ground state of H_0. The Eq.(3.58) can be rewritten as

$$\exp(-\beta\Omega) = \exp(-\beta\Omega_0)\sum_{n=0}^{\infty}\lambda^n W_n, \tag{3.59}$$

$$W_n = \frac{(-1)^n}{n!}\int_0^\beta \mathrm{d}\tau_1\cdots\int_0^\beta \mathrm{d}\tau_n \left\langle T_\tau \hat{V}(\tau_1)\cdots\hat{V}(\tau_n)\right\rangle. \tag{3.60}$$

Using the linked cluster theorem, this series can be resumed into

$$\exp(-\beta\Omega) = \exp\left\{-\beta\Omega_0 + \sum_{\ell=1}^{\infty}\lambda^\ell U_\ell\right\}, \tag{3.61}$$

$$U_\ell = \frac{(-1)^\ell}{\ell}\int_0^\beta \mathrm{d}\tau_1\cdots\int_0^\beta \mathrm{d}\tau_\ell \left\langle T_\tau \hat{V}(\tau_1)\cdots\hat{V}(\tau_\ell)\right\rangle. \tag{3.62}$$

Setting $\lambda = 1$ we get Ω as

$$\Omega = \Omega_0 - \frac{1}{\beta}\sum_{\ell=1}^{\infty}U_\ell. \tag{3.63}$$

To compute the second-order correction of the thermodynamic potential Ω, we just take U_2, the second order expansion of the S-matrix. Using the relation

$$\boldsymbol{s}_i = \frac{1}{2}c^\dagger_{i\alpha}\boldsymbol{\sigma}_{\alpha\beta}c_{i\beta}, \tag{3.64}$$

we get

$$\Delta\Omega^{(2)} = -\frac{J^2}{4\beta}\sum_{\alpha\beta\gamma\delta}\boldsymbol{S}_i\cdot\boldsymbol{\sigma}_{\alpha\beta}\boldsymbol{S}_j\cdot\boldsymbol{\sigma}_{\gamma\delta}\int_0^\beta \mathrm{d}\tau_1\int_0^\beta \mathrm{d}\tau_2\left\langle T_\tau\left\{c^\dagger_{i\alpha}(\tau_1)c_{i\beta}(\tau_1)c^\dagger_{j\gamma}(\tau_2)c_{j\delta}(\tau_2)\right\}\right\rangle. \tag{3.65}$$

Using the Wick's theorem, we can rewrite the integrand in above equation as

$$\left\langle T_\tau\left\{c^\dagger_{i\alpha}(\tau_1)c_{i\beta}(\tau_1)c^\dagger_{j\gamma}(\tau_2)c_{j\delta}(\tau_2)\right\}\right\rangle = \delta_{\beta\gamma}\delta_{\delta\alpha}\left\langle T_\tau\left\{c_{i\beta}(\tau_1)c^\dagger_{j\gamma}(\tau_2\right\}\right\rangle\left\langle T_\tau\left\{c_{i\delta}(\tau_2)c^\dagger_{j\alpha}(\tau_1\right\}\right\rangle \tag{3.66}$$

$$= -\mathcal{G}_{\beta\gamma}(i,j;\tau_1-\tau_2)\mathcal{G}_{\delta\alpha}(j,i;\tau_2-\tau_1), \tag{3.67}$$

where $\mathcal{G}$ represent the Matsubara Green's function. The presence of delta of Kronecker in the integrand of Eq. (3.65) allown to write

$$\sum_{\alpha\beta\gamma\delta}\boldsymbol{S}_i\cdot\boldsymbol{\sigma}_{\alpha\beta}\boldsymbol{S}_j\cdot\boldsymbol{\sigma}_{\gamma\delta} = \boldsymbol{S}_i\cdot\boldsymbol{S}_j, \tag{3.68}$$

and thus

$$\Delta\Omega = -J^2\chi_{ij}\boldsymbol{S}_i \cdot \boldsymbol{S}_j, \tag{3.69}$$

where

$$\chi_{ij} = -\frac{1}{4\beta}\int_0^\beta \mathrm{d}\tau\, \mathcal{G}_{\beta\gamma}(i,j;\tau)\mathcal{G}_{\delta\alpha}(j,i;-\tau); \qquad \tau = \tau_1 - \tau_2 \tag{3.70}$$

is the free electrons spin susceptibility.

Finally we can write the effective Hamiltonian as

$$H_{\mathrm{RKKY}} = -J_{\mathrm{RKKY}}\boldsymbol{S}_i \cdot \boldsymbol{S}_j, \tag{3.71}$$

$$J_{\mathrm{RKKY}} = J^2\chi_{ij}. \tag{3.72}$$

3.3.1 Kondo versus RKKY

When both the Kondo effect and the RKKY interaction are present, there is a competition between both. An important quantity that can be use d to analyze that competition is the Kondo temperature as a function of U, denoted $T_K^*(U)$, which we obtain through the Haldane expression for the Kondo temperature [44], given by

$$T_K^*(U) = 0.364\left(\frac{2\Delta U}{\pi}\right)^{1/2} \exp\left[\frac{\varepsilon_0(\varepsilon_0+U)}{2\Delta U/\pi}\right]. \tag{3.73}$$

As discussed in the previous section, when a magnetic moment is placed in a metallic host, the Kondo effect occurs, where the magnetic moment is screened by the spin of the conduction electrons, forming a many-body spin-singlet state, called Kondo cloud. The range of the Kondo cloud is greater the lower the Kondo temperature. If another magnetic moment is placed at the host, the spin of the two impurities could interact via RKKY interaction.

If the distance between the two magnetic impurities is larger than the Kondo cloud, the magnetic moment will be completely screened by the conduction electrons, and therefore the other impurity will not notice the presence of the other, so that the Kondo effect will dominate. However, if the Kondo cloud is large enough to encompass the other impurity, the RKKY interaction will dominate, as the Kondo screening was not fully implemented, and thus both impurities spin will notice each other presence [45, 46].

The presence of the Kondo effect in rare-earth metals (such as Ce, Sm, and Yb) and actinides (such as U, Np, and Pu) leads to unusual behavior in some measurements, in particular heat capacity, where, for example, the heat capacity of $CeAL_3$ is about 1600 times greater than Cu. Consequently the effective electron mass also increases, being about 1000 times the bare electron mass [37, 41], which leads to the name *heavy fermions* for those materials.

In such materials, the competition between Kondo and RKKY plays a significant role, where the Kondo coupling leads to a paramagnetic Fermi liquid state without local moments, while the RKKY interaction tends to induce magnetic order of the local moments.

4 The Lanczos transformation and DMRG

4.1 The Lanczos Transformation

4.1.1 The One Impurity Problem

The Lanczos transformation [47] is an iterative method which takes advantage of the following theorems (which will not be prove here):

Theorem 1. *Let A be a Hermitian matrix, always has an unitary matrix Q, $Q^\dagger Q = \mathbb{1}$, so that*

$$Q^\dagger A Q = T \tag{4.1}$$

where T is a Hermitian triangular matrix.

Theorem 2. *The unitary matrix Q that tridiagonalises the matrix A, is a matrix where the columns is the orthonormal Lanczos basis*

Despite the Lanczos algorithm is mostly used to find ground state of large sparse Hamiltonians (since a matrix in a tridiagonal form is more easy for some diagonalization routine to find its eigenvectors and eigenvalues), the idea in this work is to do mapping between a d-dimensional matrix into an *equivalent* chain Hamiltonian [20] in order to be used as a input for the DMRG algorithm (see sec. 4.2). Consider a Hamiltonian in the form

$$H = H_\ell + H_{\text{imp}} + V_c, \tag{4.2}$$

where, H_ℓ is a single-particle tight-binding Hamiltonian of the system. H_{imp} and V_c describe the impurity and the coupling between impurity and system, respectively.

The algorithm to tranform the Hamiltonian (4.2) into tridiagonal starts by choosing one site of the lattice, called *seed*:

$$|\psi_0\rangle = c_0^\dagger |0\rangle , \tag{4.3}$$

where $c_0^\dagger$ creates an electron ate the seed position, and $|0\rangle$ is the vacuum state. This site will be related with the impurity in two ways, one is the place where the impurity will couple to, and second, the seed itself will be the impurity.

Once the seed was chosen, the next Lanczos states will be constructed from the following iterative method:

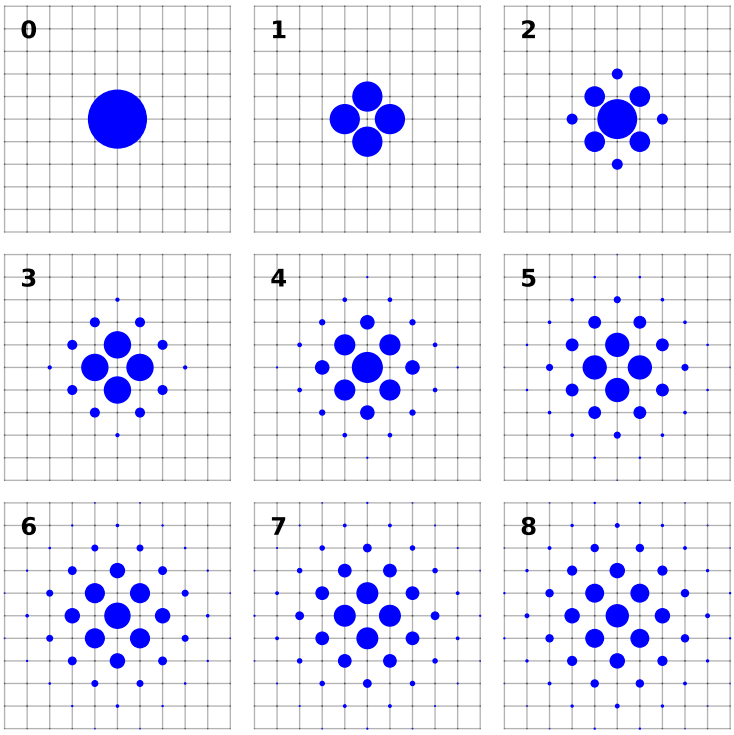

Figure 13 – Wave functions of the Lanczos states in real space in a square lattice for the first 8 iterations.

$$|\psi_1\rangle = H_\ell\,|\psi_0\rangle - a_0\,|\psi_0\rangle \tag{4.4}$$

$$|\psi_{n+1}\rangle = H_\ell\,|\psi_n\rangle - a_0\,|\psi_n\rangle - b_n^2\,|\psi_{n-1}\rangle \tag{4.5}$$

where a_0 and b_0 can be obtained by requiring the states to be orthogonal. Doing this we have

$$a_n = \frac{\langle\psi_n|H_\ell|\psi_n\rangle}{\langle\psi_n|\psi_n\rangle} \tag{4.6}$$

$$b_n^2 = \frac{\langle\psi_n|\psi_n\rangle}{\langle\psi_{n-1}|\psi_{n-1}\rangle} \tag{4.7}$$

In Fig. 13 is shown the first 8 Lanczos states for a square lattice. After the

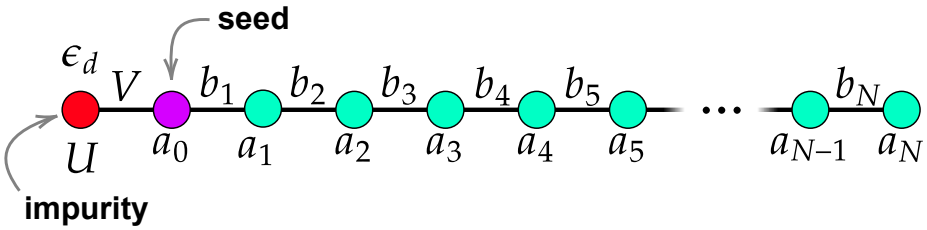

Figure 14 – Equivalent chain geometry of the transformed Hamiltonian. The red circles represent the adatom impurity, the purple the sedd and the cyan the sites of the Lanczos chain

transformation, we get a Hamiltonian in a tridiagonal form:

$$H_\ell^{\mathrm{L}} = \begin{pmatrix} a_0 & b_1 & 0 & 0 & \cdots \\ b_1 & a_1 & b_2 & 0 & \cdots \\ 0 & b_2 & a_2 & b_3 & \cdots \\ 0 & 0 & b_3 & a_3 & \cdots \\ \vdots & \vdots & \vdots & \vdots & \ddots \end{pmatrix} \tag{4.8}$$

In second quantization this matrix becomes

$$H_\ell = \sum_{i=0}^{N} a_i \tilde{n}_i + \sum_{i=0}^{N-1} b_{i+1} \left(\tilde{c}_i^\dagger \tilde{c}_{i+1} + \mathrm{h.c.} \right), \tag{4.9}$$

where $\tilde{c}_i^\dagger$ ($\tilde{c}_i$) are normalized creation (annihilation) operator for the Lanczos states, $\tilde{n}_i = \tilde{c}_i^\dagger \tilde{c}_i$ is the particles number operator, and N is the total length of the chain. In Fig. 14 is showing the resulting chain from the Lanczos transformation, where here the diagonal a_i's coefficients become the on-site potential and the b_i's the hopping along the chain.

One important thing is that, is that for large N, numerical errors arise with each iteration. To reduce the errors, re-orthogonalizion can be done using, for example, Grand-Schmidt procedure or QR decomposition (where the columns of the matrix Q will be the vector of the new orthonormalized basis).

Although the recursion can be performed until reaching the real size of the lattice, in practice the iteration are stopped before after a sufficient number of iteration. If the number of iterations is large, it may happen that the Lanczos orbitals will be reflected by the boundary of the real lattice. Once you have done this, you can reintroduce the impurity terms H_{imp} and V_c from Hamiltonian (4.2), since this has not been changed by the transformation.

4.1.2 Multiples Seeds

In the previous section we discuss how the Lanczos transformation can mapping an one-impurity problem into an equivalent chain Hamiltonian. For the situation where has more than one impurity coupled to different seeds (or even being the seeds), we use a generalization of the Lanczos algorithm, the Block Lanczos (BL) transformation. Considering again the the Hamiltonian (4.2), where the H_ℓ and V_c terms now represent the all the impurities and the coupling of the impurities with the lattice, using the BL transformation, we can mapping the Hamiltonian into an equivalent *ladder* geometry [48, 49].

As before, we start by choosing the seed states. Consider a system consisting M seeds and N single-particle sites, and thus $N + M$ being the size o the whole system (without the impurities for the adatom case). Let $|\boldsymbol{r}_1\rangle, |\boldsymbol{r}_2\rangle, \ldots, |\boldsymbol{r}_M\rangle$ be M-dimensional real apace states of the seeds, we can construct an $(N + M) \times M$ matrix Q_1 as:

$$Q_1 = (|\boldsymbol{r}_1\rangle, |\boldsymbol{r}_2\rangle, \ldots, |\boldsymbol{r}_M\rangle) \tag{4.10}$$

Here, Q_1 will be the initial BL basis. The next BL states Q_j can be generated by the recurrence,

$$A_j = Q_j^\dagger H_\ell Q_j, \tag{4.11}$$

$$Q_{j+1}B_j^\dagger = H_\ell Q_j - Q_j A_j - Q_{j-1}B_{j-1}, \tag{4.12}$$

where $Q_0 = 0$ and $B_0 = 0$. The matrices Q_{j+1} and $B_j^\dagger$ on the left-hand side of the Eq. (4.12) is obtained through the QR decomposition in the right-hand site of the Eq. (4.12). So, we have that Q_{j+1} (the Q matrix from QR decomposition) is a column $(N + M) \times M$ orthogonal matrix and B_j (the R matrix from decomposition) is a lower triangular $M \times M$ matrix. After a sufficient number L of iterations (as in the simple Lanczos transformation, there is no need to go until the real size of the system), we can construct the BL basis with and bringing them together to construct the unitary Q matrix:

$$Q = (Q_1, Q_2, \ldots, Q_L). \tag{4.13}$$

The unitary matrix Q, can used to transform the one-body part H_ℓ of the Eq. (4.2) as

$$[H_\ell^{\mathrm{BL}}]_{(ML)\times(ML)} = [Q^\dagger]_{(ML)\times(N+M)}[H_\ell]_{(N+M)\times(N+M)}[Q]_{(N+M)\times(ML)} \tag{4.14}$$

where we made a point of emphasizing the size of each matrix. The transformed matrix H_ℓ^{BL} is then a block-tridiagonal matrix:

$$H_\ell^{\mathrm{BL}} = \begin{pmatrix} A_1 & B_2 & 0 & 0 & \cdots \\ B_2 & A_2 & B_3 & 0 & \cdots \\ 0 & B_3 & A_3 & B_4 & \cdots \\ 0 & 0 & B_4 & A_4 & \cdots \\ \vdots & \vdots & \vdots & \vdots & \ddots \end{pmatrix} \tag{4.15}$$

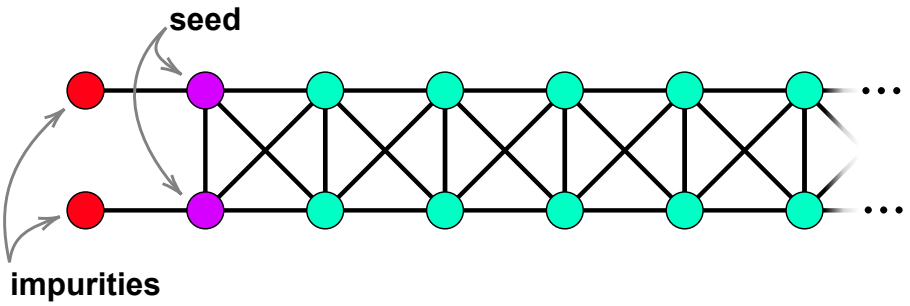

Figure 15 – Ladder geometry for a two-impurities system. The red circles indicate the adatom impurities, the purple ones are the seed, and the cyan sites of the bath of the ladder. Depending on the geometry of the lattice, some hopping (black lines) can be zero.

The Hamiltonian in the form of the Eq. (4.15) has the geometry of the ladder system, as exemplified in the Fig. 15

4.1.3 Mapping into Star Geometry

In order to increase the convergence of the DMRG, which we will see in the next section, it is useful to transform the ladder geometry system into a "star"-shaped geometry. In this geometry the seeds will remain unchanged and all the rest will be transformed in order that in this new basis, all the remaining sites (now called *bath*) will be coupled to the seeds.

Let us first describe the mapping for a single impurity, and later it would make a generalization for multiple impurities. For that, first the the Hamiltonian matrix (4.8) is split into two blocks, one containing just a seed state, which will remain unchanged, and the other the rest of the chain, as follows:

$$H_\ell^{\mathrm{L}} = \left(\begin{array}{c|cc} a_0 & b_1 & 0 \\ \hline b_1 & & \\ 0 & & H' \end{array}\right). \tag{4.16}$$

Here, b_1 is the hopping parameter between the seed state and H'. The block H' is then diagonalized, and his eigenvalues will be the site potential of the bath sites. The hopping between the seed and the bath will be $V_n = b_1 c_n$, where c_n are the values of the n^{th} eigenvector of H' at the site H'_{11} (first site of H' or second chain site). After that, the

Eq. (4.8) will be:

$$H_\ell^{\text{L, star}} = \begin{pmatrix} a_0 & V_1 & V_2 & V_3 & \cdots \\ V_1 & \varepsilon_1 & 0 & 0 & \cdots \\ V_2 & 0 & \varepsilon_2 & 0 & \cdots \\ V_3 & 0 & 0 & \varepsilon_3 & \cdots \\ \vdots & \vdots & \vdots & \vdots & \ddots \end{pmatrix} \tag{4.17}$$

For multiple impurities, the idea is straightforward. Consider a system with m seeds case. As it was done in Eq. (4.16), he Hamiltonian (4.15) is split in two as fallow

$$H_\ell^{\text{BL}} = \left(\begin{array}{c|cc} A_1 & B_2 & 0 \\ \hline B_2 & & \\ 0 & & H' \end{array}\right), \tag{4.18}$$

where now A_1 and B_2 are $m \times m$ matrix and H is a $(L-m) \times (L-m)$ matrix. Again in analogy of the Eq. (4.17), we will have

$$H_\ell^{\text{L, star}} = \begin{pmatrix} A_1 & V \\ V^\dagger & H_d \end{pmatrix} \tag{4.19}$$

where V is a $m \times L$ matrix representing the hopping between the seeds and the bath, and, H_d is the diagonalized matrix of H'. We can find the matrix elements of V as the following: let $\{|\alpha_i\rangle : i = 1, .., m\}$ be the corresponding states of the seeds, $\{|u_j\rangle : j = 1, .., L-m\}$ the basis states of the basis H' and $\{|\phi_j\rangle : j = 1, .., L-m\}$ the eigenstates of H' (in that way, the whole basis state before the star transformation is $\{|\alpha_i\rangle\} \cup \{|u_j\rangle\}$, and $\{|\alpha_i\rangle\} \cup \{|\phi_j\rangle\}$ after transformation). Defining the completion relation of H as

$$\mathbb{1} = \sum_{i=1}^{m} |\alpha_i\rangle\langle\alpha_i| + \sum_{j=1}^{L-m} |u_j\rangle\langle u_j| \,, \tag{4.20}$$

and using the fact that $\langle\alpha_i|\phi_j\rangle = 0$, we can write the matrix elements of V as:

$$\begin{aligned} \langle\alpha_i|H|\phi_j\rangle &= \langle\alpha_i|H\mathbb{1}|\phi_j\rangle \\ &= \langle\alpha_i|H\sum_{i=1}^{m}|\alpha_i\rangle\langle\alpha_i|\phi_j\rangle + \langle\alpha_i|H\sum_{j=1}^{L-m}|u_j\rangle\langle u_j|\phi_j\rangle \\ &= \sum_{j=1}^{L-m}\langle\alpha_i|H|u_j\rangle\langle u_i|\phi_j\rangle = \sum_{j=1}^{m}\langle\alpha_i|H|u_j\rangle\langle u_i|\phi_j\rangle \end{aligned}$$

where in the last step it was used that $\langle\alpha_i|H|u_j\rangle = 0$ for $j > m$.

In Fig. 16 is shown a schematic for both one and two seed star geometry.

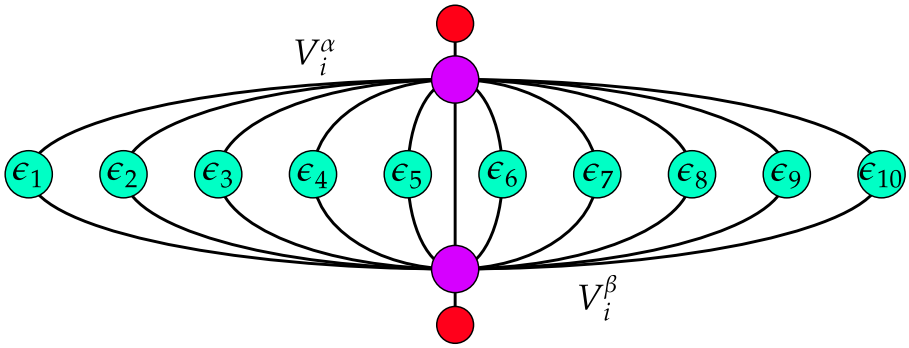

Figure 16 – Star geometry for the two impurity Anderson model. The purple circle represents the seed, the red, the adatom impurity, and the cyan is the sites of the bath which are coupled to the seed by hopping V_i^α and V_i^β.

4.2 Application of DMRG to Lanczos Transformation

4.2.1 Many Body Computational Problem

Consider that we have a Heisenberg chain and we want to solve it exactly. The Hamiltonian of this chain can be constructed by iteration, where at each iteration it added a site to the chain. If we want to diagonalize this Hamiltonian, soon we will face a big problem, as the Hilbert space $\{|\uparrow\rangle, |\downarrow\rangle\}$ for one spin ha dimension 2, at each iteration, the Hilbert space dimension increase by a 2 factor, and then, after N iteration we will be a space with dimension 2^N which is numerically very unpractical. For an electron the situation is even worse, since the basis space has four states $(|0\rangle, |\uparrow\rangle, |\downarrow\rangle, |\uparrow\downarrow\rangle)$, and thus for a system with N particles, the Hilbert space will have dimension 4^N and the Hamiltonian $4^N \times 4^N$ size. In Table 2 is shown a comparison between the memory requirement for exact diagonalization in a electronic system. We can easily perceive how the situation becomes unpractical for system with more than 8 sites.

This trouble in many body physics led to the development of many numerical

No. of sites	Hilbert space dim.	Hamiltonian size	Hamiltonian memory size
1	4	16	128 B
2	16	256	2 KB
4	256	65536	512 KB
8	65536	4.294967×10^9	32 GB
16	4.29497×10^9	1.84467×10^{19}	128 TB
32	1.84467×10^{19}	3.40282×10^{38}	2.5 EB
64	3.40282×10^{38}	1.15792×10^{77}	800 YB

Table 2 – Memory requirement for a exact diagonalization of electron's system with different sizes. As we can see for a small size with only 16 sites, the situation becomes unpratical.

methods using the most diverse approximation methods in order to deal with it. Some of them are mean-field approximation, DFT [50], quantum Monte Carlo [51], numerical renormalization group (NRG) [10, 9, 52], and others. Inspired by NRG, was proposed in 1992 by White e new method called density-matrix renormalization group (DMRG) [53], and it has been regarded as the numerical algorithm with the highest accuracy for 1D systems.

The main idea of the DMRG consists in splitting the system into two sub-system (blocks), that we will call here as *left* (L) block and *right* (R) block, where the two blocks are grown by adding one site to both blocks simultaneously until reach a desired number of state. After that it will start the truncation process, consisting in get rid the less *entangled* states. Before starting to describe with more details the algorithm, we will discuss some important concept.

4.2.2 Reduced Density Matrix

Consider $\mathcal{H} = \mathcal{H}_\mathrm{A} \otimes \mathcal{H}_\mathrm{B}$ a Hilbert space of a bipartite system composed of subsystem A and B with $\dim \mathcal{H}_\mathrm{A} = D_\mathrm{A}$ and $\dim \mathcal{H}_\mathrm{B} = D_\mathrm{B}$ (and thus $\dim \mathcal{H} = D_\mathrm{A} \times D_\mathrm{B}$), whose respective Hamiltonians are H_A and H_B, and the Hamiltonian of the global system A + B is defined as:

$$H_\mathrm{AB} = H_\mathrm{A} \otimes H_\mathrm{B}. \tag{4.21}$$

Let $\{|i,\mathrm{A}\rangle \otimes |j,\mathrm{B}\rangle\}$, with $|i,\mathrm{A}\rangle \in \mathcal{H}_\mathrm{A}$ and $|i,\mathrm{B}\rangle \in \mathcal{H}_\mathrm{B}$, be the basis state of $\mathcal{H}$. Consider now a ground state $|\psi\rangle \in \mathcal{H}$ written as:

$$|\psi\rangle = \sum_{i,j} \phi_{ij} \, |i,\mathrm{A}\rangle \otimes |j,\mathrm{B}\rangle \, . \tag{4.22}$$

Now we can construct the density matrix ρ of the ground state:

$$\rho = |\psi\rangle\langle\psi| \tag{4.23}$$

Let us introduce the reduced density matrix of the system A ρ_A, whose matrix elements can be construct as:

$$\langle i,\mathrm{A}|\rho_\mathrm{A}|i',\mathrm{A}\rangle = \sum_j \left(\langle j,\mathrm{B}| \otimes \langle i,\mathrm{A}|\right)\rho(|i',\mathrm{A}\rangle \otimes |j,\mathrm{B}\rangle) \tag{4.24}$$

The way ρ_A is construct via the Eq. (4.24) can be understood as performing the trace only in the B basis:

$$\rho_\mathrm{A} = \mathrm{Tr}_\mathrm{B}\, \rho, \tag{4.25}$$

where Tr_B is called *partial trace on B*. Similarly, the reduced density matrix of system B is:

$$\rho_\mathrm{B} = \mathrm{Tr}_\mathrm{A}\, \rho. \tag{4.26}$$

The reduced density matrix for the system A, as example, describes a mixed state in which the system A is in contact with the bath environment B. As the density matrix ρ of the whole system, the reduced density matrix has $\operatorname{Tr}\rho_{\mathrm{A}} = 1$, is Hermitian with non-negative eigenvalues λ_α, and, his eigenvector form an orthonormal basis, which implies that we can always transform the reduced density matrix into its eigenvector basis $\{|\alpha\rangle\}$:

$$\rho_{\mathrm{A}} = \sum_\alpha \lambda_\alpha |\alpha\rangle\langle\alpha| , \tag{4.27}$$

where $\lambda_\alpha \geq 0$, for all α, and $\sum_\alpha \lambda_\alpha = 1$.

4.2.3 Entanglement in quantum many-body systems

Consider again the bipartite space $\mathcal{H} = \mathcal{H}_{\mathrm{A}} \otimes \mathcal{H}_{\mathrm{B}}$, his basis state $\{|i,\mathrm{A}\rangle \otimes |j,\mathrm{B}\rangle\}$, and, let us perform the so called *Schmidt decomposition* on the ground state (4.22). This can be done by applying the SVD decomposition in the coefficients ϕ_{ij} (which defines a matrix):

$$\phi_{ij} = USV^\dagger \tag{4.28}$$

$$= \sum_\alpha^r U_{i\alpha} s_\alpha V^*_{\alpha j}, \tag{4.29}$$

with $r = \min(D_{\mathrm{A}}, D_{\mathrm{B}})$. Consequently the Eq. (4.22) becomes:

$$|\psi\rangle = \sum_i^{D_{\mathrm{A}}} \sum_j^{D_{\mathrm{B}}} \sum_\alpha U_{i\alpha} s_\alpha V^*_{\alpha j} |i,\mathrm{A}\rangle \otimes |j,\mathrm{B}\rangle \tag{4.30}$$

$$= \sum_\alpha s_\alpha \left(\sum_i U_{i\alpha} |i,\mathrm{A}\rangle \right) \otimes \left(\sum_j V^*_{\alpha j} |j,\mathrm{B}\rangle \right) \tag{4.31}$$

$$= \sum_\alpha s_\alpha |s,\mathrm{A}\rangle \otimes |s,\mathrm{B}\rangle \tag{4.32}$$

Now using $|\psi\rangle$ as defined by the Eq. (4.32), we can write the reduced density matrix as:

$$\rho_{\mathrm{A}} = \operatorname{Tr}_{\mathrm{B}} |\psi\rangle\langle\psi| = \sum_\alpha^r s_\alpha^2 |s,\mathrm{A}\rangle\langle s,\mathrm{A}| \tag{4.33}$$

$$= \sum_\alpha^r \lambda_\alpha |\alpha,\mathrm{A}\rangle\langle\alpha,\mathrm{A}| \tag{4.34}$$

where in the final step we rewrite the reduced density matrix in his own eigenbasis. The same can be done for ρ_{B}. From these results we can conclude that the eigenvalues of the reduced density matrices are $\lambda_\alpha = s_\alpha^2$, the square of the singular values, the two reduced density matrices share the spectrum, and the Schmidt bases are the eigenvectors of the reduced density matrices.

Now let the order the eigenvalues of the reduced density matrix be in decreasing order $\lambda_1 > \lambda_2 > \cdots > \lambda_m > \cdots > \lambda_r$, we can rewrite the Eq. (4.32) as

$$|\psi\rangle = \sum_{\alpha}^{r} \lambda_\alpha^{1/2} |\alpha, \mathrm{A}\rangle \otimes |\alpha, \mathrm{B}\rangle \,. \tag{4.35}$$

Now we can construct a truncated state. For this we will consider only the first $m < r$ terms of the state (4.35):

$$|\psi'\rangle = \sum_{\alpha}^{m} \lambda_\alpha^{1/2} |\alpha, \mathrm{A}\rangle \otimes |\alpha, \mathrm{B}\rangle \,, \tag{4.36}$$

and computing the Frobenius distance, defined as $\||\psi\rangle - |\psi'\rangle\|$, which will give us

$$\||\psi\rangle - |\psi'\rangle\| = \sum_{i=m+1}^{r} \lambda_i. \tag{4.37}$$

This result proves that the optimal basis is given by the eigenvectors of the reduced density matrix with the m largest eigenvalues. Considering the von-Neumann entropy $S = -\operatorname{Tr}(\rho_\mathrm{A} \log \rho_\mathrm{A})$ which measure the amount the entanglement entropy, we can rewrite it in the ρ_A eigenstates basis as:

$$S = -\sum_{\alpha}^{r} \lambda_\alpha \log \lambda_\alpha \tag{4.38}$$

$$\approx -\sum_{\alpha}^{m} \lambda_\alpha \log \lambda_\alpha \tag{4.39}$$

The result of Eq. (4.39) led us to conclude that the truncation done in Eq. (4.36) keeps only the state with the highest entanglement. This truncation is the key of the DMRG algorithm, which will be detailed described in the next section.

4.2.4 Infinite DMRG

The idea behind the infinite-size DMRG consists in split the system into two subsystems, left block and right block. We start with a small system in both blocks and start to grow each block by adding sites in both blocks at each iteration. As we add sites on the blocks, the size of the Hilbert space will grow, and after reach a desired size m (a size still possible to be exactly diagonalized) we start the DMRG truncation, in which the most entangled states will be keep. This new state will be the new system that we will restart the growing process. This can be repeated until a desired energy convergence is reached. As showed in Ref. [54] the algorithm can be more detailed described as:

- **Initialization:**

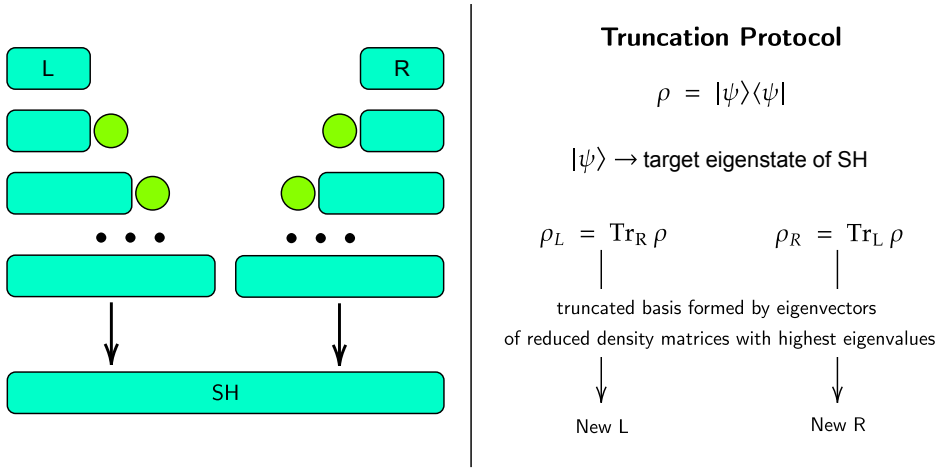

Figure 17 – Schematic representation of the infinite DMRG. The system, composed of two subsystem, grows at each iteration until reach a desirable size, and then the two subsystem is joined into a single system forming a super-Hamiltonian (SH). The truncation protocol starts by first building the density matrix with the eigenstates of SH; the two reduced density matrix is then built and the truncation is done by keeping the eigenvectors of both reduced density matrix with highest eigenvalues. The Hamiltonian and operators of both subsystem is now transformed into the new basis, resulting in a new block for which the process will be repeated.

1. Construct all operator matrices for a single site within the system, including those involved in interactions between the site and the rest of the system.
2. Begin the process by incrementally adding single sites to the blocks.
3. Assuming the Hilbert space for a single site has dimension d, once the block sizes exceed $d \times m$, we initiate the application of density matrix truncation

- **Density Matrix Truncation Procedure:**

1. Diagonalize the full Hamiltonian (Using a suitable library routine like Lanczos or Davidson) of the two blocks combined, to obtain the ground state $|\psi\rangle = \sum_{i,j} \phi_{ij} |i, \mathrm{A}\rangle \otimes |j, \mathrm{B}\rangle$.
2. Compute the reduced density matrices for both the left and right blocks.
3. For each block, diagonalize its density matrix to obtain the full spectrum of eigenvalues and their corresponding eigenvectors.
4. Reduce the basis size by retaining only the m eigenvectors associated with the largest eigenvalues.
5. Transform the Hamiltonian and the operators involved in interactions between the blocks to the new, truncated basis.
6. Incorporate a new site into both the left and right blocks, resulting in new blocks with dimensions of $d \times m$. Repeat the diagonalization and truncation

steps iteratively. This process continues until the desired system size is reached or the error in the energy falls below a predetermined tolerance level.

The infinite DMRG procedure is summarized in Fig. 17

During the initial development of DMRG, it was believed that this method would provide a reliable approximation of a system's characteristics as it approached an infinite size. However, current understanding suggests that the optimal approach to reach the thermodynamic limit involves employing the finite-size algorithm on systems with a fixed length as will be discussed in next section.

4.2.5 Finite DMRG

As in the infinite-size algorithm, the finite-size algorithm split the system into two block, left and right, but while one block will be increase by adding a site, the other will be decrease by removing a site, in order to keep the total size of system unchanged. The finite-size DMRG can be summarized as follows:

- **Initialization:**
  1. Execute the infinite-size algorithm until the desired system size is attained. During this process, preserve the corresponding operators and basis transformations for each step. This initial stage is often referred to as the "warm-up" phase.
  2. Once the desired system size is reached, we initiate a process known as "DMRG sweeps" to enhance the accuracy of the results. These sweeps involve alternating between left-to-right and right-to-left sweeps.
- **Left-to-Right Sweep Process:**
  1. Expand the left block by incorporating a site from the system. To maintain a constant overall system size, the right block must be reduced in size. This can be achieved by utilizing the smaller right block from the infinite-size step or from the previous right-to-left sweep.
  2. Employ a suitable library routine (such as Lanczos or Davidson) to diagonalize the combined Hamiltonian of the two blocks. This process is identical to the one used in the infinite-size DMRG.
  3. Compute the reduced density matrix of the left block.
  4. Diagonalize the density matrix to obtain its eigenvalues and eigenvectors.
  5. Truncate the basis by retaining only the eigenvectors associated with the largest eigenvalues, thus reducing the dimensionality of the problem.

6. Transform the Hamiltonian and the operators of the left block involved in interactions between the blocks to the new basis.
7. Repeat steps 1-6, iteratively moving towards the right end of the system until the right block contains only a single site. This completes one left-to-right sweep

- **Right-to-Left Sweep Process:**

1. Perform a sweep in the opposite direction, from right to left, by incrementally expanding the right block and shrinking the left block. The left block configuration is initialized using the result from the previous left-to-right sweep.

- **Iteration and Convergence:**

1. Continue alternating between left-to-right and right-to-left sweeps until the change in energy falls below a predefined threshold. Typically, the process stops when both blocks reach the same size, resulting in a "symmetric configuration".

The infinite DMRG is schematically depicted in Fig. 18. The iterative sweeping process employed in the DMRG functions is akin to a self-consistent loop, progressively refining the solution with each iteration. In essence, DMRG can be understood as a variational method in which the parameters are continuously optimized to minimize an energy functional.

All this discussion of the DMRG applies only for one-dimensional systems. If we happen to want to use the DMRG on a 2D or 3D system, we have to make a transformation

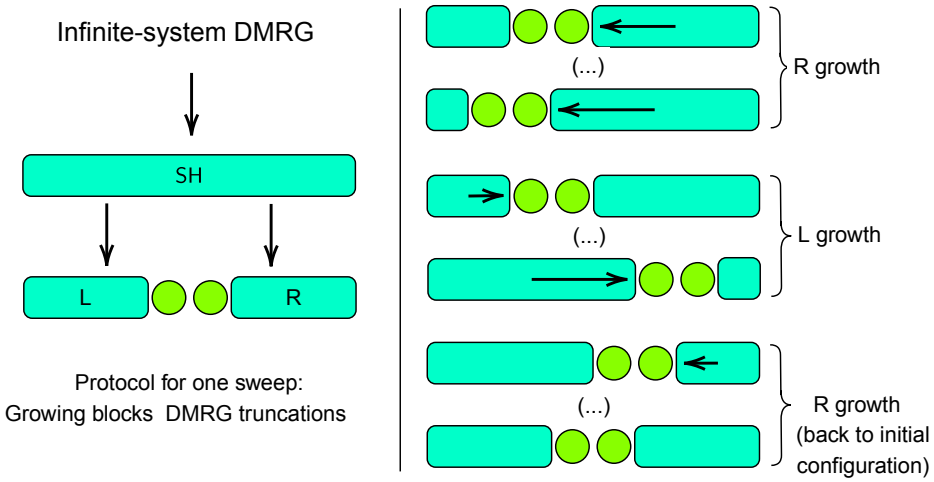

Figure 18 – Schematic representation of the finite DMRG. Once reaching the size of the system in the infinite DMRG, we begin the sweep protocol, where the whole system is again split into two subsystems, where at each iteration, one grows while the other shrinks, and the truncation protocol is applied. This is done until the smaller subsystem reach the smallest size, and then the reversed process begins.

of the 2D (3D) Hamiltonian in a effective 1D Hamiltonian. There are many ways to do that, and in this work we made use of the Lanczos tridiagonalization and Block-Lanczos tridiagonalization for this purpose.

5 Results

5.1 DMRG Convergence Analysis

Although quite effective, DMRG can become a bit confusing to work with. That happens due to many parameters that we can manipulate, like the cutoff number of states and the number of sweeps, the minimum tolerance. In addition since its development, various works has been done to discuss and improve the performance of the DMRG [55, 56, 57]. In another works are proposed "tricks" in order to achieve better results in convergence like orbital relaxation protocol [58, 59] and optimal ordering of orbitals [60, 61].

However sometimes, choose the best parameter in order to achieve the best performance can be a little tricky. In this work, we analyze some of the main DMRG parameters in order to understand the best configuration of these parameters.

Firstly, we start by applying the DMRG to a single-particle Hamiltonian of a silicene zigzag nanoribbon. This being single particle Hamiltonian, can therefore be easily exact diagonalized, where the exact ground state energy will be used to compare with the DMRG results. For a particle hole symmetric Hamiltonian, the ground state can be obtained by summing the first half of the eigenvalues obtained through the subroutine. The first analysis that we performed was to compare the performance between both ladder and star geometry. In Fig. 19 is showed the the difference δE between the exact ground state energy with the DMRG results as function of the cutoff number of states. We can clearly notice that the star geometry is much more accurate, where we can see that even for 50 number of states, the star geometry has a energy variance less than 0.05. Still in the same image, we can also compare the running time for each code. This shows us that the running time of the ladder geometry is faster than the star geometry for the same number of cutoff states, however, since the star geometry requires more number of states, we ended up taking more time to achieve the same convergence of the star geometry. Because of this, all remaining results in this section were done using the star geometry.

Focus on the star geometry, we analyze the convergence and the running time for different number of sweeps. Fig. 20 shows the variation energy δE for different number of sweeps. In these results we can see huge increase in the rate of convergence between the changing of 6 sweeps to 10 sweeps. However, the increase in convergence in the variation between 10 and 14 sweeps is completely negligible. Analyzing the time of running, we can verify that, for a small number of states, the time is almost identical, but with the increase of the number of states, the time starts to grow exponentially, and the rate of increase in time grows with the number of sweeps, as expected.

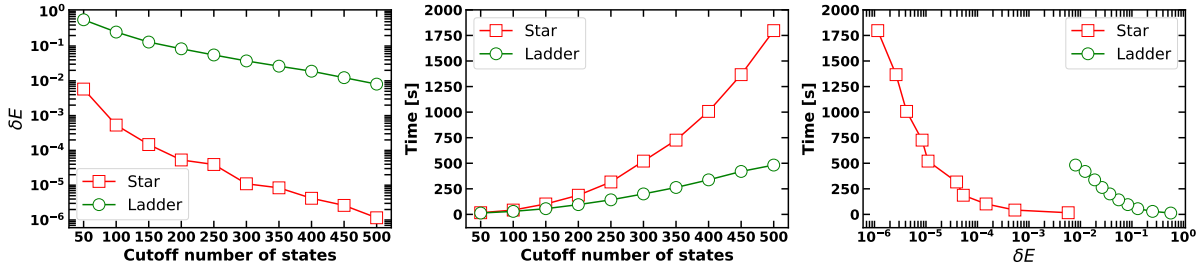

Figure 19 – At left: variation between the exact ground state energy and the obtained by DMRG as a function of the cutoff number states for both star and ladder geometries; at middle: the running time for both star and ladder geometry as a function the cutoff number states; at right: the running time for both star and ladder geometry as a function the energy variation. Although the time of running of the ladder geometry grows slowly when compared to the star, the fact that the star geometry leads to a faster convergence makes the time of running of the ladder higher than the star

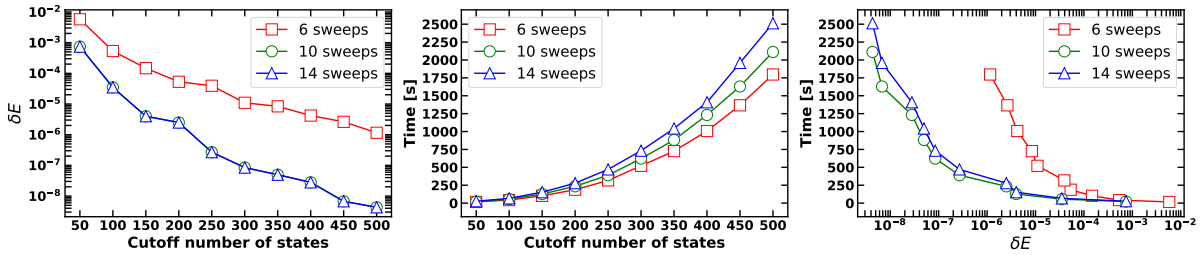

Figure 20 – At left: variation between the exact ground state energy and the obtained by DMRG as a function of the cutoff number state for star geometry using different number of sweeps; at middle: the running time for star geometry as a function the cutoff number states. The increase of number of sweeps increase the convergence significantly when changes from 8 to 10. But when change from 10 to 14, any change is noticeable; at right: the running time for both star and ladder geometry as a function the energy variation.

For the interactive case, as we cannot solve exactly, we chose to check the convergence by comparing the occupations and the correlations, and comparing some results with those present in Ref. [1]. These results were obtained in a siliciene zigzag nanoriboon with a single substitutional impurity. Except when specified, all results below is for a system with 64 sites, $\lambda_{\mathrm{SO}} = 0.1$, $U = 4.0$, $\varepsilon_d = -2.0$ and $V = 0.65$.

Fig. 21 shows the occupation for a system with 300 states and with different number of sweeps. We can see that for a small number of sweeps, the region close to the Fermi level is filled with a series of messy points, which the width of this region decrease with the increase of number of sweeps. For 12 sweeps begins to appear close to the Fermi-Dirac distribution, which is expected for the ground state of a fermionic system. Thus we can use the occupation as a parameter of convergence. Still in this figure, we can see that in the 12 sweeps case, the presence of two states far from $\langle n \rangle \approx 2$ and $\langle n \rangle \approx 0$, representing the many-body states where the electron on the impurity is constantly scattered to the

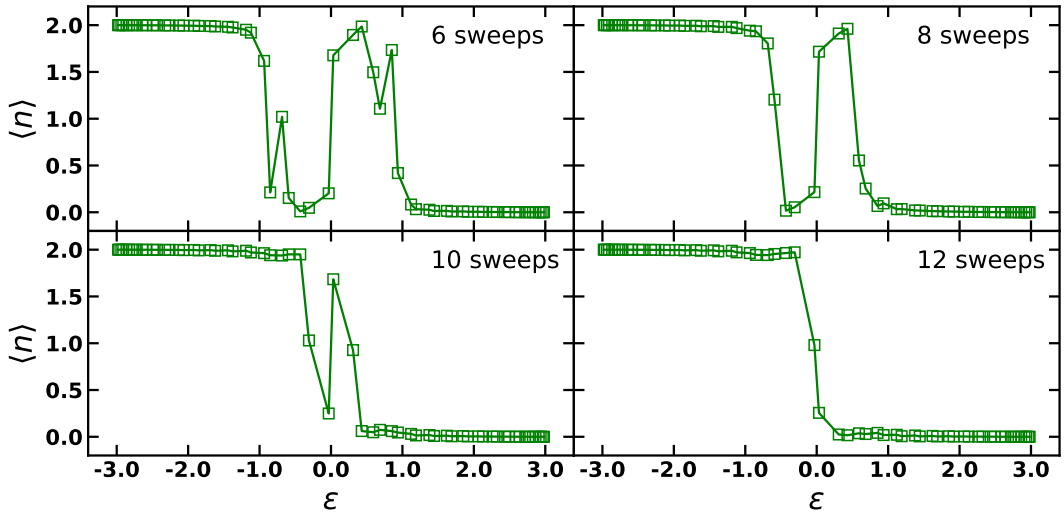

Figure 21 – Occupation of the ground state for four different number of sweeps. For a not-converged result, we can see a messy of point around the Fermi level. When the results begin to converge, the occupation begins to appear close to the Fermi-Dirac distribution.

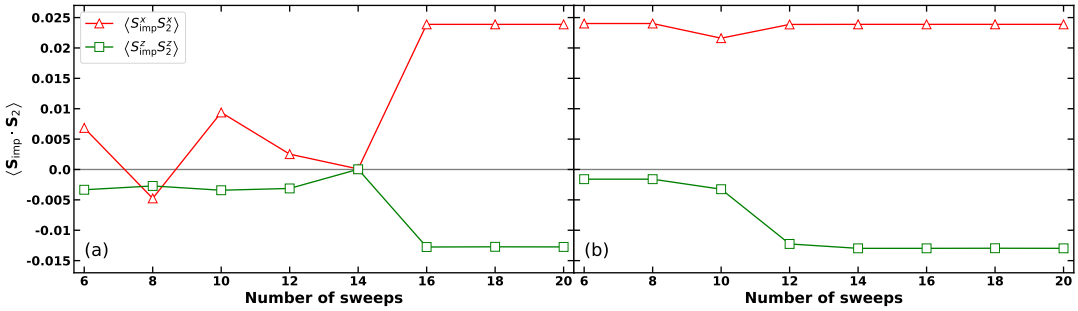

Figure 22 – Comparison between the convergence rate for the spin correlation $\langle S^z_{\text{imp}} S^z_j \rangle$ and $\langle S^x_{\text{imp}} S^x_j \rangle$ between the substitutional impurity at the crest position with a site at the edge two sites of distance as function of the number of sweeps, with 300 states. In panel (a), is showed the results without any nose, while in the panel (b) with have the results with a nose of 1×10^{-3}, which was turned off after the 4th, 6th and 8th sweeps for the cases for 6 sweeps, 8 sweeps, and more than 8 sweeps respectively.

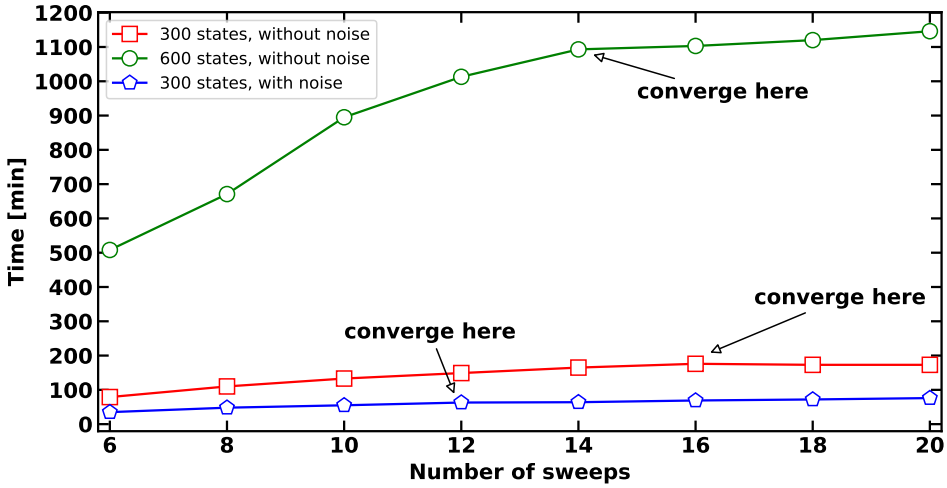

Figure 23 – Comparison between the running time between, for the with (blues squares) and without (red square and green circles) noise with 300 states. We can clearly see how the noise increase dramatically the convergence, converging faster than the case for 600 states in less time than the situations with 300 states without noise.

Fermi level.

It is possible that the DMRG fails to find the true ground state and get stuck in a metastable state [62], due the lose of some state during the warm-up. In order to avoid it, we can add a small amount of noise to the reduced density matrix at each step; this is done by constructing the density matrix from

$$(1-\delta)\,|\psi_0\rangle + \delta\,|\chi\rangle\,, \tag{5.1}$$

where $|\psi_0\rangle$ is the eigenstate of the super-Hamiltonian, δ is a small number and $|\chi\rangle$ is a random eigenstate. This noise is generally turned off in subsequent sweeps [63]. In Fig. 22(a))and 22(b) we have two graphics showing the correlations $\langle S^z_{\text{imp}} S^z_j \rangle$ and $\langle S^x_{\text{imp}} S^x_j \rangle$ between the impurity and a site at the edge of two distance sites, with 300 states. The noise is 1×10^{-3} and it was turned off after the 4th sweep, for the case with 6 sweeps. after the 6th sweeps for the 8 sweeps case and after the 8th sweeps for the remaining cases with more than 8 sweeps. In both Fig. 22(b) and 22(b) we have the correlation as a function of the number of sweep, but in Fig. 22(b) is used the noise trick, while in the Fig.. 22(a) does not. We can easily check that the presence of noise increase the convergence of the result. Fig. 23 shows the running time for a system with 300 states, using the noise trick, and two systems with 300 and 600 states without noise. This result show us how the use of the noise can improve drastically the convergence and the running time for the code, where the 300 states case with noise converge faster than the 300 states case without noise, and with less number of sweeps than the 600 states without noise case.

5.2 RKKY effect in silicene

The following figures present our spin correlation results between one impurity coupled to a crest site on a silicene edge and another impurity coupled to a site that moves away from the crest, starting at the adjacent trough site, up to a distance of 10 lattice spacings (see Fig. 24). All results are for 3 different U values ($U = 4$, 2.4, and 1.2), and we present results for $\lambda_{SO} = 0.0$ and 0.1 (see panels (a) and (b), respectively, in Fig. 25). The coupling of the impurities is kept fixed at $V = 0.65$, and we are at the particle-hole symmetric (PHS) point, $\varepsilon_d = -U/2$. We also display an estimate of the Kondo temperature for each U value, denoted $T_K^*(U)$, which we obtain through the Haldane expression for the Kondo temperature (see Eq. (3.73)), whose expression for PHS case is given by

$$T_K^*(U) = 0.364\left(\frac{2\Delta U}{\pi}\right)^{1/2} \exp\left[\frac{-\pi U}{8\Delta}\right], \tag{5.2}$$

where $\Delta = \pi V^2 \rho(0)$, being $\rho(0)$ the host density of states at the Fermi energy (which we take as being 1).

Starting with Fig. 25(a), where we have results for $\langle S_1 \cdot S_2 \rangle$, for different values of U and the vanishing SOC, we first see the usual alternance of AF/F in the correlations between the impurities, indicating the expected sign change for J_{RKKY} as the impurities gradually separate. It is also clear that, for a lower Kondo temperature (larger U) the strength of the RKKY interaction (the magnitude of J_{RKKY}) decreases and falls with distance more slowly.

Turning on the SOC interaction ($\lambda_{SO} = 0.1$), we see in Fig. 25(a), a dramatic increase in the AF correlation at distance 1 for $U = 4$ (red squares curve), while there

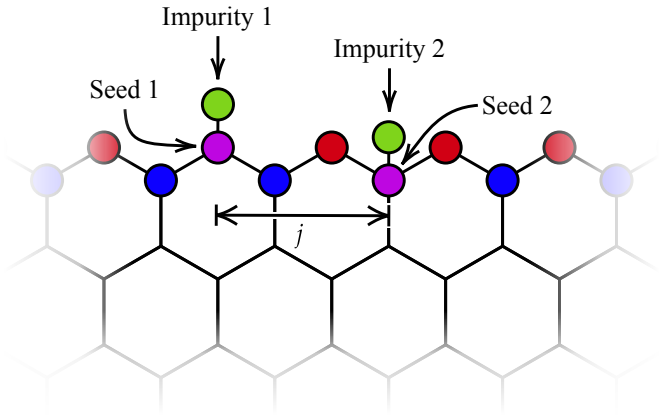

Figure 24 – Schematic representation of the system configuration. The violet circles represents the seeds of the Block-Lanczos algorithm, while the green ones represents the adatom impurities. In this configuration, seed 1 (and impurity 1) is fixed, and the seed 2 (and impurity 2) is moved away at distance j and computed its correlation via DMRG.

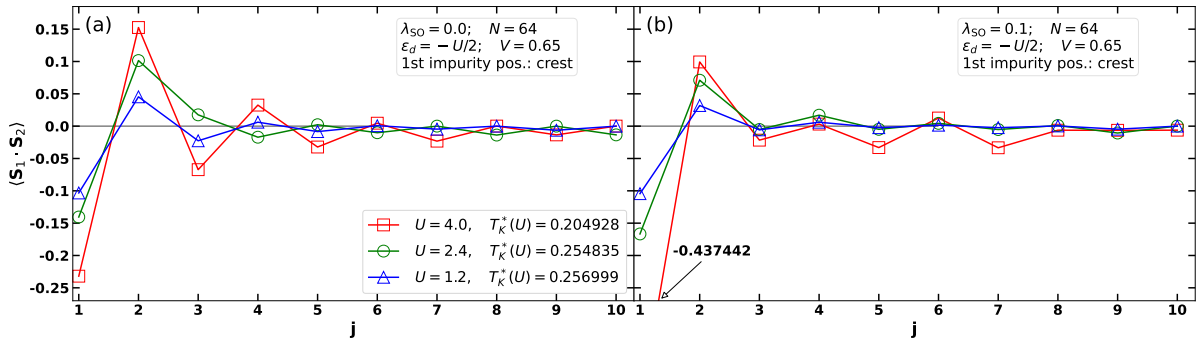

Figure 25 – Spin correlations for an adatom impurity to a crest edge site for values $U = 4.0$ (red squares), 2.4 (green circles), and 1.2 (blue triangles) as a function of distance j between the impurities. Panel (a) is for a ribbon with vanishing SOC and panel (b) for a ribbon with $\lambda_{\rm SOC} = 0.1$. The parameters are $V = 0.65$ and $\varepsilon_d = -U/2$ (PHS point). It can be easily seen in both panels, that the impurities more correlated as the Kondo temperature decreases (larger U vales). In addition, the presence of SOC decreases the range of the RKKY interaction and greatly increases the AF correlation at distance 1 for $U = 4.0$. These results were obtained through DMRG using 500 states and 30 sweeps.

is a much smaller change (at distance 1) for the smaller U values. It is also clear that a finite SOC decreases the range of the RKKY interaction, since now the magnitude of the correlations falls faster with distance.

A finite SOC breaks SU(2) symmetry, thus we expect some anisotropy in the spin correlations for the $\lambda_{SO} = 0.1$ results. Indeed, we obtain that $\langle S_1^x \cdot S_2^x \rangle = \langle S_1^y \cdot S_2^y \rangle \neq \langle S_1^z \cdot S_2^z \rangle$. This can be observed in panels (a) to (c), in Fig. 26, for $U = 4$, 2.4, and 1.2, respectively. Note that, since $\langle S_1^x \cdot S_2^x \rangle = \langle S_1^y \cdot S_2^y \rangle$, we show just $\langle S_1^x \cdot S_2^x \rangle$ (dashed lines) in all three panels in Fig. 26. Since the silicene nanoribbon is in the xy plane, we will call $\langle S_1^z \cdot S_2^z \rangle$ the out-of-plane (OP) correlations, and the other correlations will be called in-plane (IP) correlations. A comparison of the three panels, indicates that there is a qualitative change in passing from $U = 4$ [panel (a)] to $U = 2.4$ [panel (b)]. Indeed, for the lower $T_K^*(U)$ (higher U) the OP correlations dominate, having a larger magnitude and a much longer reach. This trend is reversed for the lower Kondo temperatures [panels (b) and (c)].

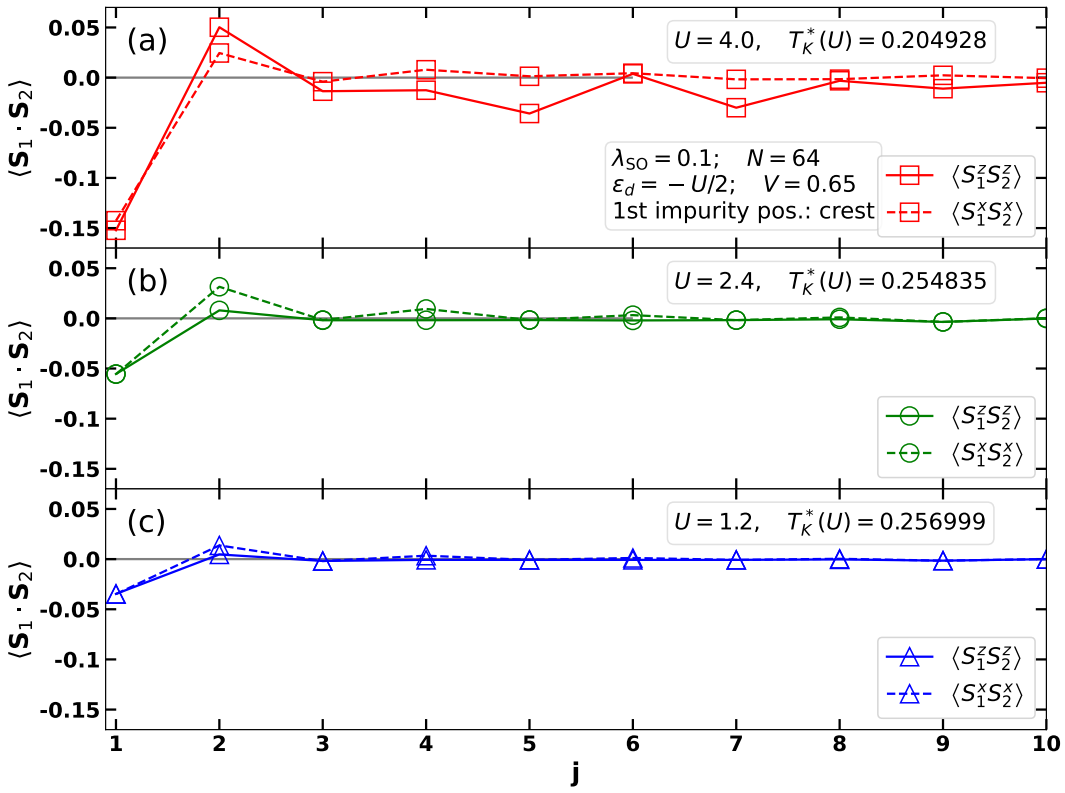

Figure 26 – Spin correlations for each spin component as function of distance j, for $\lambda_{\mathrm{SOC}} = 0.1$ and (a) $U = 4.0$, (b) $U = 2.4$, and (c) $U = 1.2$. (since $\langle S_1^x S_2^x \rangle = \langle S_1^y S_2^y \rangle$, the y-component result is not shown). As expected, the presence of SOC breaks SU(2) symmetry, resulting in anisotropy in the spin correlations. For smaller $T_K^*(U)$, as in the panel (a), the OP correlation dominates the IP, while for larger $T_K^*(U)$ as the case of the panel (b) and (c) the IP correlations dominate the OP.

6 Conclusions and perspectives

In Chapter 4, we have seen that the RKKY interaction increases, both in magnitude as in range, when the Kondo temperature decreases, both for a topologically trivial nanoribbon and for a non-trivial one. However, for the non-trivial nanoribbon, we noticed a few interesting effects. First, for the lowest Kondo temeprature analyzed, the AF correlation between side by side impurities almost doubles [red squares in Fig. 25(b)], when compared to the vanishing SOC result. There is just a slight increase in the magnitude of the corresponding correlations for higher Kondo temperatures [green circles and blue triangles in Fig. 25(b)]. In addition, for higher Kondo temperatures, SOC clearly decreases the range of the RKKY interaction, while the decrease in the range of the RKKY interaction, for the smallest value of the Kondo temperature is much less prominent.

As to the anisotropy introduced by SOC, which is reflected in $\langle S_1^x \cdot S_2^x \rangle = \langle S_1^y \cdot S_2^y \rangle \neq \langle S_1^z \cdot S_2^z \rangle$, we observe again a qualitative difference in the results for the lowest Kondo temperature, when compared to the higher Kondo temperature results. Indeed, for $U = 4.0$ (lowest Kondo temperature) the OP correlations dominate the IP correlations, showing a much larger range. The situation is reversed for the higher Kondo temperature results, although the difference between OP and IP correlations is not as striking as for the lowest Kondo temperature results.

As a perspective for a possible continuation of this work would be the introduction of disorder at the edge of the nanoribbon, by, for example, introducing a random potential at the sites between the impurities. One would expect that the RKKY interaction would be less affected in the topologically non-trivial system.

In the analyses of the DMRG convergence, the perspective would comparing the convergence to another system as the two impurities used in the work, test tricks proposed by Refs. [58, 59, 60, 61], and comparing performance among the most popular DMRG packages.

Bibliography

1 ALLERDT, A.; FEIGUIN, A. E.; MARTINS, G. B. Spatial structure of correlations around a quantum impurity at the edge of a two-dimensional topological insulator. *Phys. Rev. B*, v. 96, p. 035109, 2017. Disponível em: <https://link.aps.org/doi/10.1103/PhysRevB.96.035109>.

2 HEWSON, A. C. *The Kondo Problem to Heavy Fermions*. Cambridge University Press, 1993. Cambridge Books Online. Disponível em: <http://dx.doi.org/10.1017/CBO9780511470752>.

3 De Haas, W.; Van Den Berg, G. The electrical resistance of gold and silver at low temperatures. *Physica*, v. 3, n. 6, p. 440, 1936. Disponível em: <https://www.sciencedirect.com/science/article/pii/S0031891436800093>.

4 KONDO, J. Resistance minimum in dilute magnetic alloys. *Prog. Theor. Phys.*, v. 32, n. 1, p. 37, 1964. Disponível em: <https://doi.org/10.1143/PTP.32.37>.

5 ANDERSON, P. W. Localized magnetic states in metals. *Phys. Rev.*, v. 124, p. 41, 1961. Disponível em: <https://link.aps.org/doi/10.1103/PhysRev.124.41>.

6 BULLA, R.; COSTI, T. A.; PRUSCHKE, T. Numerical renormalization group method for quantum impurity systems. *Rev. Mod. Phys.*, v. 80, p. 395, 2008. Disponível em: <https://link.aps.org/doi/10.1103/RevModPhys.80.395>.

7 de Haas, W.; de Boer, J.; van den Berg, G. The electrical resistance of gold, copper and lead at low temperatures. *Physica*, v. 1, p. 1115, 1934. Disponível em: <https://doi.org/10.1016/S0031-8914(34)80310-2>.

8 SCHRIEFFER, J. R.; WOLFF, P. A. Relation between the Anderson and Kondo Hamiltonians. *Physic. Rev.*, v. 149, p. 491, 1966. Disponível em: <https://link.aps.org/doi/10.1103/PhysRev.149.491>.

9 WILSON, K. G. The renormalization group: Critical phenomena and the kondo problem. *Rev. Mod. Phys.*, v. 47, p. 773, 1975. Disponível em: <https://link.aps.org/doi/10.1103/RevModPhys.47.773>.

10 KRISHNA-MURTHY, H.; WILKINS, J.; WILSON, K. Renormalization-group approach to the Anderson model of dilute magnetic alloys. I. Static properties for the symmetric case. *Physic. Rev. B*, v. 21, p. 1003, 1980. Disponível em: <https://link.aps.org/doi/10.1103/PhysRevB.21.1003>.

11 KRISHNA-MURTHY, H.; WILKINS, J.; WILSON, K. Renormalization-group approach to the Anderson model of dilute magnetic alloys. II. Static properties for the asymmetric case. *Physic. Rev. B*, v. 21, p. 1044, 1980. Disponível em: <https://link.aps.org/doi/10.1103/PhysRevB.21.1044>.

12 STEWART, G. R. Heavy-fermion systems. *Rev. Mod. Phys.*, v. 56, p. 755, 1984. Disponível em: <https://link.aps.org/doi/10.1103/RevModPhys.56.755>.

13 KIRCHNER, S. *et al.* Colloquium: Heavy-electron quantum criticality and single-particle spectroscopy. *Rev. Mod. Phys.*, v. 92, p. 011002, 2020. Disponível em: <https://link.aps.org/doi/10.1103/RevModPhys.92.011002>.

14 ANDRES, K.; GRAEBNER, J. E.; OTT, H. R. $4f$-Virtual-bound-state formation in $CeAl_3$ at low temperatures. *Phys. Rev. Lett.*, v. 35, p. 1779, 1975. Disponível em: <https://link.aps.org/doi/10.1103/PhysRevLett.35.1779>.

15 RUDERMAN, M. A.; KITTEL, C. Indirect exchange coupling of nuclear magnetic moments by conduction electrons. *Phys. Rev.*, v. 96, p. 99, 1954. Disponível em: <https://link.aps.org/doi/10.1103/PhysRev.96.99>.

16 KASUYA, T. A theory of metallic ferro-and antiferromagnetism on Zener's model. *Prog. Theor. Phys.*, v. 16, p. 45, 1956. Disponível em: <https://doi.org/10.1143/PTP.16.45>.

17 YOSIDA, K. *Theory of magnetism*. [S.l.]: Springer Science & Business Media, 1996. v. 122.

18 JONES, B. A.; VARMA, C. M.; WILKINS, J. W. Low-temperature properties of the two-impurity Kondo Hamiltonian. *Phys. Rev. Lett.*, v. 61, p. 125, 1988. Disponível em: <https://link.aps.org/doi/10.1103/PhysRevLett.61.125>.

19 JONES, B. A.; VARMA, C. M. Critical point in the solution of the two magnetic impurity problem. *Phys. Rev. B*, v. 40, p. 324, 1989. Disponível em: <https://link.aps.org/doi/10.1103/PhysRevB.40.324>.

20 ALLERDT, A.; FEIGUIN, A. E. A numerically exact approach to quantum impurity problems in realistic lattice geometries. *Frontiers in Physics*, Frontiers Media SA, v. 7, p. 67, 2019. Disponível em: <https://doi.org/10.3389/fphy.2019.00067>.

21 BAIBICH, M. N. *et al.* Giant magnetoresistance of (001)fe/(001)cr magnetic superlattices. *Phys. Rev. Lett.*, v. 61, p. 2472, 1988. Disponível em: <https://link.aps.org/doi/10.1103/PhysRevLett.61.2472>.

22 BINASCH, G. *et al.* Enhanced magnetoresistance in layered magnetic structures with antiferromagnetic interlayer exchange. *Phys. Rev. B*, v. 39, p. 4828, 1989. Disponível em: <https://link.aps.org/doi/10.1103/PhysRevB.39.4828>.

23 YEVTUSHENKO, O. M.; YUDSON, V. I. Kondo Impurities Coupled to a Helical Luttinger Liquid: RKKY-Kondo Physics Revisited. *Phys. Rev. Lett.*, v. 120, p. 147201, 2018. Disponível em: <https://link.aps.org/doi/10.1103/PhysRevLett.120.147201>.

24 FERRER, P. A.-C.; YEVTUSHENKO, O. M.; WEICHSELBAUM, A. RKKY to Kondo crossover in helical edge of a topological insulator. *Phys. Rev. Res.*, v. 5, p. 033016, 2023. Disponível em: <https://link.aps.org/doi/10.1103/PhysRevResearch.5.033016>.

25 VOIT, J. A brief introduction to Luttinger liquids. *AIP Conference Proceedings*, v. 544, p. 309, 2000. Disponível em: <https://doi.org/10.1063/1.1342524>.

26 PADOVA, P. D. *et al.* Evidence of graphene-like electronic signature in silicene nanoribbons. *Appl. Phys. Lett.*, v. 96, n. 26, p. 261905, 2010. Disponível em: <https://doi.org/10.1063/1.3459143>.

27 AUFRAY, B. *et al.* Graphene-like silicon nanoribbons on Ag(110): A possible formation of silicene. *Appl. Phys. Lett.*, v. 96, n. 18, p. 183102, 2010. Disponível em: <https://doi.org/10.1063/1.3419932>.

28 CAHANGIROV, S. *et al.* Two- and one-dimensional honeycomb structures of silicon and germanium. *Phys. Rev. Lett.*, v. 102, p. 236804, 2009. Disponível em: <https://link.aps.org/doi/10.1103/PhysRevLett.102.236804>.

29 LIU, C.-C.; FENG, W.; YAO, Y. Quantum spin hall effect in silicene and two-dimensional germanium. *Phys. Rev. Lett.*, v. 107, p. 076802, 2011. Disponível em: <https://link.aps.org/doi/10.1103/PhysRevLett.107.076802>.

30 BERNEVIG, B. A.; ZHANG, S.-C. Quantum spin hall effect. *Phys. Rev. Lett.*, v. 96, p. 106802, 2006. Disponível em: <https://link.aps.org/doi/10.1103/PhysRevLett.96.106802>.

31 KANE, C. L.; MELE, E. J. Z_2 topological order and the quantum spin hall effect. *Phys. Rev. Lett.*, v. 95, p. 146802, 2005.

32 KANE, C. L.; MELE, E. J. Quantum spin hall effect in graphene. *Phys. Rev. Lett.*, v. 95, p. 226801, 2005. Disponível em: <https://link.aps.org/doi/10.1103/PhysRevLett.95.226801>.

33 YAO, Y. *et al.* Spin-orbit gap of graphene: First-principles calculations. *Phys. Rev. B*, v. 75, p. 041401, 2007. Disponível em: <https://link.aps.org/doi/10.1103/PhysRevB.75.041401>.

34 BERNEVIG, B. A.; HUGHES, T. L.; ZHANG, S.-C. Quantum spin hall effect and topological phase transition in hgte quantum wells. *Science*, v. 314, n. 5806, p. 1757–1761, 2006. Disponível em: <https://www.science.org/doi/abs/10.1126/science.1133734>.

35 EZAWA, M. Monolayer topological insulators: Silicene, germanene, and stanene. *J. Phys. Soc. Jpn.*, v. 84, n. 12, p. 121003, 2015. Disponível em: <https://doi.org/10.7566/JPSJ.84.121003>.

36 NETO, A. H. C.; GUINEA, F.; PERES, N. M. R. Edge and surface states in the quantum hall effect in graphene. *Phys. Rev. B*, v. 73, p. 205408, 2006. Disponível em: <https://link.aps.org/doi/10.1103/PhysRevB.73.205408>.

37 COLEMAN, P. *Introduction to many-body physics*. [S.l.]: Cambridge University Press, 2015.

38 ANDERSON, P. W. Localized magnetic states in metals. *Phys. Rev.*, v. 124, p. 41, 1961. Disponível em: <https://link.aps.org/doi/10.1103/PhysRev.124.41>.

39 EL-BATANOUNY, M. *Advanced quantum condensed matter physics: one-body, many-body, and topological perspectives*. [S.l.]: Cambridge University Press, 2020.

40 PHILLIPS, P. *Advanced solid state physics*. [S.l.]: Cambridge University Press, 2012.

41 MAHAN, G. D. *Many-particle physics*. [S.l.]: Springer Science & Business Media, 2013.

42 YOSIDA, K. Magnetic properties of Cu-Mn alloys. *Phys. Rev.*, v. 106, p. 893, 1957. Disponível em: <https://link.aps.org/doi/10.1103/PhysRev.106.893>.

43 KOGAN, E. Rkky interaction in graphene at finite temperature. *C*, v. 5, n. 2, 2019. Disponível em: <https://www.mdpi.com/2311-5629/5/2/14>.

44 HALDANE, F. D. M. Theory of the atomic limit of the anderson model. i. perturbation expansions re-examined. *Journal of Physics C: Solid State Physics*, v. 11, n. 24, p. 5015, 1978. Disponível em: <https://dx.doi.org/10.1088/0022-3719/11/24/030>.

45 SØRENSEN, E. S.; AFFLECK, I. Scaling theory of the kondo screening cloud. *Phys. Rev. B*, v. 53, p. 9153, 1996. Disponível em: <https://link.aps.org/doi/10.1103/PhysRevB.53.9153>.

46 BÜSSER, C. A. *et al.* Numerical analysis of the spatial range of the kondo effect. *Phys. Rev. B*, v. 81, p. 045111, 2010. Disponível em: <https://link.aps.org/doi/10.1103/PhysRevB.81.045111>.

47 LANCZOS, C. An iteration method for the solution of the eigenvalue problem of linear differential and integral operators. United States Governm. Press Office Los Angeles, CA, 1950.

48 SHIRAKAWA, T.; YUNOKI, S. Block lanczos density-matrix renormalization group method for general anderson impurity models: Application to magnetic impurity problems in graphene. *Phys. Rev. B*, v. 90, p. 195109, 2014. Disponível em: <https://link.aps.org/doi/10.1103/PhysRevB.90.195109>.

49 ALLERDT, A. *et al.* Kondo versus indirect exchange: Role of lattice and actual range of rkky interactions in real materials. *Phys. Rev. B*, v. 91, p. 085101, 2015. Disponível em: <https://link.aps.org/doi/10.1103/PhysRevB.91.085101>.

50 KOHN, W.; SHAM, L. J. Self-consistent equations including exchange and correlation effects. *Phys. Rev.*, v. 140, p. A1133, 1965. Disponível em: <https://link.aps.org/doi/10.1103/PhysRev.140.A1133>.

51 FOULKES, W. M. C. *et al.* Quantum monte carlo simulations of solids. *Rev. Mod. Phys.*, v. 73, p. 33, 2001. Disponível em: <https://link.aps.org/doi/10.1103/RevModPhys.73.33>.

52 BULLA, R.; COSTI, T. A.; PRUSCHKE, T. Numerical renormalization group method for quantum impurity systems. *Rev. Mod. Phys.*, v. 80, p. 395, 2008. Disponível em: <https://link.aps.org/doi/10.1103/RevModPhys.80.395>.

53 WHITE, S. R. Density-matrix algorithms for quantum renormalization groups. *Phys. Rev. B*, v. 48, p. 10345, 1993. Disponível em: <https://link.aps.org/doi/10.1103/PhysRevB.48.10345>.

54 FEIGUIN, A. E. The Density Matrix Renormalization Group and its time-dependent variants. In: . [s.n.], 2011. v. 1419, n. 1, p. 5. Disponível em: <https://doi.org/10.1063/1.3667323>.

55 LEGEZA, O.; FÁTH, G. Accuracy of the density-matrix renormalization-group method. *Phys. Rev. B*, v. 53, p. 14349, 1996. Disponível em: <https://link.aps.org/doi/10.1103/PhysRevB.53.14349>.

56 LEGEZA, O.; SÓLYOM, J. Optimizing the density-matrix renormalization group method using quantum information entropy. *Phys. Rev. B*, v. 68, p. 195116, 2003. Disponível em: <https://link.aps.org/doi/10.1103/PhysRevB.68.195116>.

57 WHITE, S. R. Density matrix renormalization group algorithms with a single center site. *Phys. Rev. B*, v. 72, p. 180403, 2005. Disponível em: <https://link.aps.org/doi/10.1103/PhysRevB.72.180403>.

58 MA, Y.; MA, H. Assessment of various natural orbitals as the basis of large active space density-matrix renormalization group calculations. *J. Chem. Phys.*, v. 138, n. 22, p. 224105, 2013. ISSN 0021-9606. Disponível em: <https://doi.org/10.1063/1.4809682>.

59 GHOSH, D. *et al.* Orbital optimization in the density matrix renormalization group, with applications to polyenes and β-carotene. *J. Chem. Phys.*, v. 128, n. 14, p. 144117, 2008. ISSN 0021-9606. Disponível em: <https://doi.org/10.1063/1.2883976>.

60 MORITZ, G.; HESS, B. A.; REIHER, M. Convergence behavior of the density-matrix renormalization group algorithm for optimized orbital orderings. *J. Chem. Phys.*, v. 122, n. 2, 2005. Disponível em: <https://doi.org/10.1063/1.1824891>.

61 ZGID, D.; NOOIJEN, M. The density matrix renormalization group self-consistent field method: Orbital optimization with the density matrix renormalization group method in the active space. *J. Chem. Phys.*, v. 128, n. 14, p. 144116, 2008. ISSN 0021-9606. Disponível em: <https://doi.org/10.1063/1.2883981>.

62 DUKELSKY, J. *et al.* Equivalence of the variational matrix product method and the density matrix renormalization group applied to spin chains. *Europhysics Letters*, v. 43, n. 4, p. 457, 1998. Disponível em: <https://dx.doi.org/10.1209/epl/i1998-00381-x>.

63 CHAN, G. K.-L.; HEAD-GORDON, M. Highly correlated calculations with a polynomial cost algorithm: A study of the density matrix renormalization group. *The Journal of chemical physics*, v. 116, n. 11, p. 4462, 2002. Disponível em: <http://dx.doi.org/10.1063/1.1449459>.